International Journal of Plasticity 171 (2023) 103802



Contents lists available at ScienceDirect

International Journal of Plasticity

journal homepage: www.elsevier.com/locate/ijplas





Discrete dislocation dynamics simulations of ⟨*a*⟩-type prismatic loops in zirconium

Daniel Hortelano-Roig [a,*], Rakesh Kumar [b], Daniel S. Balint [b], Edmund Tarleton [c,a]

[a] Department of Materials, University of Oxford, Parks Road, OX1 3PH, UK
[b] Department of Mechanical Engineering, Imperial College London, Exhibition Road, SW7 2AZ, UK
[c] Department of Engineering Science, University of Oxford, Parks Road, OX1 3PJ, UK

ARTICLE INFO

Keywords:
Discrete dislocation dynamics
Prismatic loops
Zirconium
Irradiation hardening
Dislocation channelling

ABSTRACT

Neutron irradiation of zirconium alloys in light water nuclear reactors generates nano-scale defects in the form of vacancy and interstitial ⟨*a*⟩-type prismatic loops which lie in prismatic planes of the sample. The dynamics of idealised conservative square ⟨*a*⟩-type prismatic loops have been investigated for a range of loop lengths in the framework of linear isotropic elasticity. Three-dimensional dislocation dynamics (DD) simulations of a dislocation-loop interaction have been performed to investigate the dislocation-loop interaction mechanism. For this purpose, a mobility law developed for hexagonally close-packed materials has been implemented and described in detail. Analytical and numerical calculations have been performed to obtain expressions for the restoring force and angular stability of prismatic loops. These analyses have been used to inform a 2.5D discrete dislocation plasticity (DDP) model in order to emulate realistic prismatic loop physics and improve irradiation hardening simulations. From the 2.5D DDP prismatic loop analyses, it has been observed that the stable angle of smaller sized loops is less sensitive to external stresses compared to that of larger loops, which may have implications for the mechanisms of irradiation hardening. Furthermore, initial 2.5D single-slip simulations predict that prismatic loops cause significantly elevated flow stress that increases with increasing loop density in accord with experimental observations, and that the restraining effect of the out-of-plane loop segments (the restoring force) plays an important role in the strengthening caused by loops.

1. Introduction

Due to its low absorption cross-section for thermal neutrons and good corrosion resistance, zirconium (Zr) is the primary component of the material comprising the cladding tubes in the fuel assemblies of light water reactors (LWRs) (Xu et al., 2015; Duan et al., 2017). At normal LWR operating temperatures (less than approximately 700 K), Zr exhibits a hexagonally close-packed (HCP) α-phase (Duan et al., 2017). In the reaction core, Zr is subjected to fast neutron irradiation at energies $E > 1$ MeV (Onimus and Béchade, 2012). The neutrons interact elastically with the atoms in the Zr crystal and displace them from their equilibrium positions, creating point defects without transmutation. This leads to a high density distribution of dislocation loop defects in the sample. Radiation damage of Zr alloys at low neutron fluences (less than 3×10^{25} m^{-2} for $E > 1$ MeV) has been shown to generate mostly ⟨*a*⟩-type prismatic loops on prismatic habit planes (Northwood et al., 1979). A typical Zr alloy cladding with a thickness of

* Corresponding author.
E-mail address: daniel.hortelanoroig@materials.ox.ac.uk (D. Hortelano-Roig).

https://doi.org/10.1016/j.ijplas.2023.103802
Received 3 August 2023; Received in revised form 5 October 2023
Available online 11 November 2023
0749-6419/© 2023 The Authors. Published by Elsevier Ltd. This is an open access article under the CC BY license (http://creativecommons.org/licenses/by/4.0/).

less than a millimetre which receives a fast neutron flux of $5 \times 10^{17}\ \mathrm{m^{-2}\,s^{-1}}$ may receive this upper bound of fast neutron fluence in approximately two years (Onimus and Béchade, 2012).

The microstructure and corresponding characteristics of distributed prismatic loops in neutron-irradiated Zr alloys has a complex dependence on irradiation temperature, purity, and thermo-mechanical history of the sample. At the low neutron fluences and temperatures as similar to those seen at LWR operating conditions, neutron irradiation-induced prismatic loops lie on prismatic planes distributed between 1st ($\{10\bar{1}0\}$) and 2nd ($\{11\bar{2}0\}$) order prismatic planes. They have perfect $1/3\langle 11\bar{2}0\rangle$ Burgers vectors distributed equally among the three $\langle a\rangle$-type directions. It has also been found experimentally that the normal vector of the habit plane of these prismatic loops may have a small basal component (Kelly and Blake, 1973). They are distributed as both interstitial and vacancy-type loops, with the proportion depending on the irradiation temperature. They are in general elliptical in shape, with eccentricities depending on the loop size, irradiation temperature, and on whether the loops are of interstitial or vacancy-type. For instance, in one "round-robin" study of nuclear-grade Zr alloys, at irradiation temperatures ranging from 523–673 K it was found that loop diameters ranged from 8.5–20 nm and loop densities were approximately on the order of $1 \times 10^{22}\ \mathrm{m^{-3}}$ (Northwood et al., 1979). The aforementioned study will contribute to the motivation of the computational parameters used for this paper. See Onimus and Béchade (2012) for a review of the microstructural evolution in irradiated Zr alloys.

It is well known that prismatic loops act as obstacles to dislocation motion (Kroupa and Hirsch, 1964; Kubin and Kratochvil, 2000), which leads to hardening in the irradiated material (Higgy and Hammad, 1972; Adamson, 2000). For a sufficiently high applied stress, dislocations can overcome the prismatic loop barriers. This results in the formation of defect-free channels facilitating further dislocation motion, leading to plastic strain localisation (Luft, 1991). In combination with other irradiation-induced phenomena, these dislocation channels can have a significant impact on the properties of irradiated Zr, such as in early material fracture (Yagnik and Garde, 2019). In unirradiated Zr alloys, the prismatic slip systems are the preferred planes for dislocation glide (Tenckhoff, 1988). However, when irradiated, the preferred glide planes become the basal slip systems (Onimus et al., 2004; Onimus et al., 2013). This has been associated with a greater increase in the critical resolved shear stress of prismatic slip systems compared to basal slip systems after irradiation. In addition, it has been shown on a statistical basis that dislocations gliding on basal slip systems have a greater probability of triggering loop-clearing mechanisms compared to dislocations gliding on prismatic slip systems (Drouet et al., 2014).

In order to obtain a better understanding of irradiation hardening, the interactions between gliding dislocations and defect clusters such as prismatic loops has been the subject of much recent numerical investigation. Dislocation-defect interactions involve mechanisms which operate at multiple length scales, and have consequently been modelled using both molecular dynamics (MD) and dislocation dynamics (DD) simulations. At the atomic scale, individual dislocation-defect interactions have been classified and described extensively by Bacon and Osetsky (2005) and Bacon et al. (2009). MD simulations of dislocations interacting with prismatic loops have been performed in face-centred cubic (FCC) metals (Rodney, 2004; Borde et al., 2023), body-centred cubic (BCC) metals (Nomoto et al., 2005; Bacon et al., 2006; Liu and Biner, 2008; Terentyev et al., 2008), and, of particular relevance to this paper, HCP Zr (Voskoboynikov et al., 2005; Serra and Bacon, 2013). At the mesoscopic scale, DD simulations have been performed to investigate dislocation-loop interactions in FCC (Erel et al., 2017; Borde et al., 2023), BCC (Shi et al., 2015), and HCP (Drouet et al., 2014) metals.

In the literature it is understood from analytical (Bacon, 1966; Wolfer et al., 2004), atomistic (Serra and Bacon, 2013; Dai et al., 2017), and experimental (Kelly and Blake, 1973; Jostsons et al., 1977; Mussi et al., 2021) analyses that the tilt angle between the habit plane normal vector and Burgers vector of prismatic dislocation loops tends to adopt a stable point which is influenced by the presence of external stress fields. The precise mechanism of prismatic loop tilting and stability is currently not fully understood. The tilt angle of prismatic loops has a significant impact on their interaction with other dislocations (Wolfer et al., 2004). The stability of the prismatic loop habit plane may depend on the loop size, loop shape, and the degree of material anisotropy. To the knowledge of the authors of this paper, to date there exists no studies in the literature which systemically compute stable loop tilt angles as a function of loop sizes.

Dislocation dynamics is a continuum model of material plasticity on the order of micrometres which treats dislocation line defects explicitly as discretised segments embedded within an elastic medium (Groh and Zbib, 2009; Sills et al., 2016; Zhuang et al., 2019). There are several computational challenges associated with this approach. Three-dimensional (3D) DD simulations must be capable of modelling complex physics at a mesoscopic scale (Sills and Aubry, 2018). Additionally, 3D DD must achieve a sufficient level of computational efficiency required to model plastic strains large enough to understand macroscopic bulk plastic deformation behaviour. 3D DD simulations have a large computational cost, making parallelisation essential for large-scale simulations. Directly computing the interactions between N dislocation segments is expensive, with order $\mathcal{O}\left(N^2\right)$ scaling. In addition, the number of nodes and segments must change during run-time in order to achieve a balance between accuracy and performance; finding the optimal topological operations can be challenging. Although advances in 3D DD have increased feasible plastic strains, most modern 3D DD simulations are only capable of achieving relative plastic strains of $\Delta\epsilon/\epsilon < 0.5\%$ for a reasonable set of initial conditions (Arsenlis et al., 2007). Without parallelisation, modelling materials with beyond 10^5 dislocation segments at large strains would take prohibitively large amounts of computing time (Arsenlis et al., 2007). This would correspond to a dislocation density of approximately $10^{12}\ \mathrm{m^{-2}}$; for comparison, typical dislocation densities during large strain, irradiation-induced hardening conditions are approximately 10^{14}–$10^{15}\ \mathrm{m^{-2}}$ (Ribis et al., 2008).

On the other hand, planar (2D) dislocation dynamics, often referred to as discrete dislocation plasticity (DDP), is computationally faster and inherently flexible with respect to boundary conditions and the inclusion of microstructures, hence can be used to solve more complicated boundary value problems that may otherwise be inaccessible to 3D methods (Balint et al., 2005; Deshpande et al., 2006; Tarleton et al., 2015; Giessen and Needleman, 1995); dislocation structures and interactions are also more readily identified,

elucidating mechanisms and scaling relationships. That said, DDP can only be used on problems where the planarity assumption is appropriate, or otherwise mitigated by the inclusion of 2.5D information (i.e., an approximate representation of features of 3D dislocation mechanics within a planar framework). The general DDP model typically considers dislocations as infinitely long, straight, edge-type dislocations with line direction perpendicular to the plane of the simulation; planar screw-only, and edge-only coupled to screw-only models are also possible (Reali et al., 2021). The present work aims, in part, to inform an otherwise planar model of discrete edge dislocations interacting with 2D representations of irradiation loop defects with the essential 3D mechanics of dislocation-loop interactions, for a 2.5D model with sufficient fidelity to identify the salient mechanisms of irradiation hardening. In the planar model, irradiation loops are represented as planar cuts of square prismatic loops, which are captured by edge dislocation dipoles in climb configurations. For the case of the loop habit plane being perpendicular to the simulation plane, all four loop segments cannot be explicitly modelled due to the planar nature of DDP. However, the effect of the loop edge segments that are parallel to the simulation plane on the mobility of the loop segments that intersect the simulation plane can be captured by the analytical expressions derived in this work, the accuracy of which is tested against 3D simulations.

The HCP crystallography exhibited by α-Zr necessitates the use of an HCP mobility law for implementation in 3D DD. An HCP mobility law has been developed by Aubry et al. (2016) with a framework which has already been utilised in DD studies (Srivastava and El-Awady, 2017; Li et al., 2023). However, there is only one study which outlines its implementation, and here we aim to provide more detail on this method. Therefore, an additional important aim of this paper is to elucidate and elaborate upon this HCP mobility law in order to facilitate its wider use and potential modification in future studies.

The sections of this paper are outlined as follows. In Section 2, the 3D DD simulation method used is described, including the mobility law necessitated by the HCP crystallography. In Section 3, the results of a 3D simulation between an edge dislocation and a prismatic loop are described and discussed. In Section 4, the stability of a 3D prismatic loop is discussed and an analytical expression for its restoring force is presented. In Section 5, the 3D restoring force is implemented into a 2.5D DD model and the consequences are described and discussed.

2. Methods

2.1. 3D DD formulation

In this paper, 3D DD simulations were performed using EasyDD, which is a MATLAB-based code developed at the University of Oxford (University of Oxford Materials, 2021). EasyDD uses node-based discretisation, incorporates GPU acceleration, and is capable of modelling finite domains. EasyDD is based on the 3D DD code ParaDiS, which is written mostly in C and developed at Lawrence Livermore National Laboratory by Arsenlis et al. (2007). In EasyDD, the smooth dislocation structure is represented as a nodal network C consisting of a set of nodes $\{n_k\}$ and piecewise straight segments $\{\Gamma_{ij}\}$, each of which connects node n_i at position $\boldsymbol{x}_i$ to node n_j at position $\boldsymbol{x}_j$. Each segment generates an elastic stress field which influences every other segment in a pairwise fashion, resulting in an N-body problem that must be solved. The Peach–Koehler force $\boldsymbol{f}^{\mathrm{PK}}$ may then be evaluated along each segment. Although the segments represent the conceptual picture, the computations themselves are performed on the nodes.

The elastic force on node n_i is calculated via

$$\boldsymbol{f}_i^{\mathrm{e}} = \oint_C N_i(\boldsymbol{x})\, \boldsymbol{f}^{\mathrm{PK}}(\boldsymbol{x})\, \mathrm{d}L(\boldsymbol{x}) \tag{1}$$

where the integral is performed over the entire nodal network C. The shape functions $N_i(\boldsymbol{x})$ used by EasyDD are linear, and are defined along each segment as

$$N_i(\boldsymbol{x}) = \frac{|\boldsymbol{x} - \boldsymbol{x}_j|}{|\boldsymbol{x}_i - \boldsymbol{x}_j|} \tag{2}$$

such that $N_i(\boldsymbol{x})$ varies linearly from $N_i(\boldsymbol{x}_i) = 1$ to $N_i(\boldsymbol{x}_j) = 0$ (Bulatov and Cai, 2006). This method allows one to account for the field contributions to n_i due to all of its connected segments. Since the classical stress field expressions exhibit singularities at the dislocation core (Hirth and Lothe, 1982), they are unsuitable for computational implementation. EasyDD instead uses the non-singular continuum elastic theory stress expressions derived by Cai et al. (2006) at the cost of requiring one additional input parameter: the isotropic Burgers vector spreading radius r_c.

The local atomic configuration surrounding the dislocation core stores a short-ranged inelastic energy which can be expressed as

$$\mathcal{E}^c = \sum_{\text{all segments}} \epsilon^c(\boldsymbol{b}_{ij}, \boldsymbol{l}_{ij}) |\boldsymbol{L}_{ij}| \tag{3}$$

where $\boldsymbol{L}_{ij} = \boldsymbol{x}_j - \boldsymbol{x}_i$ is the segment length vector and $\epsilon^c(\boldsymbol{b}_{ij}, \boldsymbol{l}_{ij})$ is the non-negative, empirically-determined core energy per unit length for a segment with a given Burgers vector $\boldsymbol{b}_{ij}$ and unit line vector $\boldsymbol{l}_{ij} = \boldsymbol{L}_{ij}/|\boldsymbol{L}_{ij}|$. The core energy gives rise to short-ranged core forces which can be derived by computing the negative gradient of the core energy. Performing this differentiation for a single isolated segment Γ_{ij} yields the core force contribution to node n_i due to its connection to node n_j given by

$$\boldsymbol{f}_{ij}^c = \epsilon^c(\boldsymbol{b}_{ij}, \boldsymbol{l}_{ij}) \boldsymbol{l}_{ij} + \left(I - \boldsymbol{l}_{ij} \otimes \boldsymbol{l}_{ij}\right) \cdot \frac{\partial \epsilon^c(\boldsymbol{b}_{ij}, \boldsymbol{l}_{ij})}{\partial \boldsymbol{l}_{ij}} \tag{4}$$

where I is the 3×3 identity matrix. The first and second terms in Eq. (4) represent the longitudinal and torsional core forces, respectively. EasyDD uses an expression for the core energy density ϵ^c which smoothly interpolates between regimes defined by fitting parameters given by

$$\epsilon^c(\theta) = \frac{E_s^c}{1-\nu}\left(1 - \nu\cos^2\theta\right) \tag{5}$$

where θ is the character angle. The empirical parameter E_s^c is the core energy per unit length of a screw dislocation and is related to the core energy per unit length of an edge dislocation E_e^c via the phenomenological relation $E_s^c = E_e^c(1-\nu)$. These relations are inspired by the expressions for the elastic strain energy density of infinitely long mixed dislocations, which are similar in form and interpolation.

The nodal forces result in nodal kinematics, and the induced nodal velocities are determined by the mobility law. The mobility law used in this paper is based off of the one described by Aubry et al. (2016), and its implementation is described in detail in Section 2.2. Note that this mobility law is built upon the ParaDiS framework discussed above. After the mobility module, the time integrator solves for the updated nodal positions. Finally, topological operations (which proceed according to energy minimisation arguments) are performed to determine the result of dislocation collision and separation reactions (Bulatov and Cai, 2006; Arsenlis et al., 2007).

2.2. Mobility law for HCP materials

2.2.1. HCP crystallography

The geometry of the HCP crystal may be described by the Miller-Bravais system, which denotes families of planes using the four indices $(hkil)$ such that $h + k + i = 0$ (Hull and Bacon, 2011a). The direct HCP lattice vectors are conventionally defined as the linearly dependent set of vectors given by

$$\begin{aligned}
\boldsymbol{a}_1 &= a\left(-\frac{1}{2}\hat{\boldsymbol{x}} + \frac{\sqrt{3}}{2}\hat{\boldsymbol{y}}\right)\\
\boldsymbol{a}_2 &= a\left(-\frac{1}{2}\hat{\boldsymbol{x}} - \frac{\sqrt{3}}{2}\hat{\boldsymbol{y}}\right)\\
\boldsymbol{a}_3 &= a\hat{\boldsymbol{x}}\\
\boldsymbol{a}_4 &= c\hat{\boldsymbol{z}}
\end{aligned} \tag{6}$$

where $\hat{\boldsymbol{x}}$, $\hat{\boldsymbol{y}}$, and $\hat{\boldsymbol{z}}$ are the unit Cartesian basis vectors, and a and c are the two HCP lattice parameters. The redundant index i facilitates the identification of symmetries present in the HCP system. Therefore, a given set of Miller-Bravais indices denotes the family of planes perpendicular to the normal vector which may be constructed via

$$\boldsymbol{n} = h\boldsymbol{a}_1^* + k\boldsymbol{a}_2^* + l\boldsymbol{a}_4^* \tag{7}$$

where $\{\boldsymbol{a}_1^*, \boldsymbol{a}_2^*, \boldsymbol{a}_4^*\}$ denotes the dual basis corresponding to the direct basis $\{\boldsymbol{a}_1, \boldsymbol{a}_2, \boldsymbol{a}_4\}$. The notation $[hkil]$ refers to a vector $\boldsymbol{b}$ expressed as a linear combination of the direct HCP lattice vectors via

$$\boldsymbol{b} = h\boldsymbol{a}_1 + k\boldsymbol{a}_2 + i\boldsymbol{a}_3 + l\boldsymbol{a}_4 \tag{8}$$

Table 1 contains all the possible HCP slip systems (i.e. all combinations of Burgers and normal vectors) considered in this paper. See Fig. 1 for a visualisation of all the slip systems and corresponding slip planes. The notation for plane types used in this paper is based on the notation used by Aubry et al. (2016), which consists of an integer referring to the glissile Burgers vector, followed by a combination of letters and Roman numerals which refer to the slip plane. There are five different slip plane types considered: $\{0001\}$ basal (Ba), $\{10\bar{1}0\}$ prismatic (Pr), $\{10\bar{1}1\}$ primary pyramidal type I (PyI), $\{10\bar{1}1\}$ primary pyramidal type II (PyII), and $\{11\bar{2}2\}$ secondary pyramidal (sP). The three types of Burgers vectors — $\langle a\rangle$, $\langle a{+}c\rangle$, and $\langle c\rangle$ — are labelled according to the lattice parameters which must be used to describe them, and respectively correspond to Burgers vectors $\boldsymbol{b}_1$ to $\boldsymbol{b}_3$, $\boldsymbol{b}_4$ to $\boldsymbol{b}_9$, and $\boldsymbol{b}_{10}$ in Table 1. Note that these slip systems are all included for completeness; only the 2Ba and 2Pr slip systems are required for the 3D simulations performed in this paper. In addition, the 2.5D simulations performed in this paper only require prismatic slip systems, and do not currently use the HCP mobility law described in this section.

2.2.2. Dislocation kinematics

Given a complete set of nodal forces acting on the dislocation network, the resulting nodal kinematics must be computed in order to determine the dislocation dynamics. The response of each node depends on local fields such as stress, temperature, pressure, and the line, Burgers, and normal vectors of its connected segments. In general, this leads to nonlinear nodal equations of motion which must be solved by a mobility law.

The dislocation core response to forces depends on inelastic atomistic interactions which cannot be directly modelled by the linear elastic theory. In order to incorporate these atomic-scale effects into linear elasticity, mesoscopic theories of dislocation mobility have been derived with a set of free parameters which are empirically determined from finer-scale theories. For instance, MD simulations can be performed in which dislocation velocities are calculated as functions of a given stress state for different dislocation orientations.

Table 1
HCP slip systems. $\rho = c/a$ represents the HCP axes ratio. The Cartesian representation of the Burgers vector is expressed as $\boldsymbol{b}_i/a$.

Burgers vector		Normal vector		Plane type
Miller-Bravais	Cartesian	Miller-Bravais	Cartesian	
$\boldsymbol{b}_1 = 1/3\left[2\bar{1}\bar{1}0\right]$	$\left[-\frac{1}{2}, \frac{\sqrt{3}}{2}, 0\right]$	$\left(0001\right)$	$\left[0,0,1\right]$	1Ba
		$\left(01\bar{1}0\right)$	$\left[-\frac{\sqrt{3}}{2}, -\frac{1}{2}, 0\right]$	1Pr
		$\left(01\bar{1}1\right)$	$\left[-\sqrt{3}\rho, -\rho, \sqrt{3}\right] / \sqrt{3+4\rho^2}$	1PyI
		$\left(0\bar{1}11\right)$	$\left[\sqrt{3}\rho, \rho, \sqrt{3}\right] / \sqrt{3+4\rho^2}$	1PyII
$\boldsymbol{b}_2 = 1/3\left[\bar{1}\bar{1}20\right]$	$\left[1,0,0\right]$	$\left(0001\right)$	$\left[0,0,1\right]$	2Ba
		$\left(1\bar{1}00\right)$	$\left[0,1,0\right]$	2Pr
		$\left(1\bar{1}01\right)$	$\left[0,2\rho,\sqrt{3}\right] / \sqrt{3+4\rho^2}$	2PyI
		$\left(\bar{1}101\right)$	$\left[0,-2\rho,\sqrt{3}\right] / \sqrt{3+4\rho^2}$	2PyII
$\boldsymbol{b}_3 = 1/3\left[\bar{1}2\bar{1}0\right]$	$\left[-\frac{1}{2}, -\frac{\sqrt{3}}{2}, 0\right]$	$\left(0001\right)$	$\left[0,0,1\right]$	3Ba
		$\left(\bar{1}010\right)$	$\left[\frac{\sqrt{3}}{2}, -\frac{1}{2}, 0\right]$	3Pr
		$\left(\bar{1}011\right)$	$\left[\sqrt{3}\rho, -\rho, \sqrt{3}\right] / \sqrt{3+4\rho^2}$	3PyI
		$\left(10\bar{1}1\right)$	$\left[-\sqrt{3}\rho, \rho, \sqrt{3}\right] / \sqrt{3+4\rho^2}$	3PyII
$\boldsymbol{b}_4 = 1/3\left[2\bar{1}\bar{1}3\right]$	$\left[-\frac{1}{2}, \frac{\sqrt{3}}{2}, 0\right]$	$\left(01\bar{1}0\right)$	$\left[-\frac{\sqrt{3}}{2}, -\frac{1}{2}, 0\right]$	4Pr
		$\left(\bar{1}011\right)$	$\left[\frac{\sqrt{3}}{2}, -\frac{1}{2}, 0\right]$	4PyI
		$\left(\bar{1}101\right)$	$\left[0,-2\rho,\sqrt{3}\right] / \sqrt{3+4\rho^2}$	4PyII
		$\left(\bar{2}112\right)$	$\left[\rho, -\sqrt{3}\rho, 2\right] / \sqrt{4+4\rho^2}$	4sP
$\boldsymbol{b}_5 = 1/3\left[2\bar{1}\bar{1}\bar{3}\right]$	$\left[-\frac{1}{2}, \frac{\sqrt{3}}{2}, -\rho\right]$	$\left(01\bar{1}0\right)$	$\left[-\frac{\sqrt{3}}{2}, -\frac{1}{2}, 0\right]$	5Pr
		$\left(10\bar{1}1\right)$	$\left[-\sqrt{3}\rho, \rho, \sqrt{3}\right] / \sqrt{3+4\rho^2}$	5PyI
		$\left(1\bar{1}01\right)$	$\left[0,2\rho,\sqrt{3}\right] / \sqrt{3+4\rho^2}$	5PyII
		$\left(2\bar{1}\bar{1}2\right)$	$\left[-\rho, \sqrt{3}\rho, 2\right] / \sqrt{4+4\rho^2}$	5sP
$\boldsymbol{b}_6 = 1/3\left[\bar{1}\bar{1}23\right]$	$\left[1,0,\rho\right]$	$\left(1\bar{1}00\right)$	$\left[0,0,1\right]$	6Pr
		$\left(10\bar{1}1\right)$	$\left[-\sqrt{3}\rho, \rho, \sqrt{3}\right] / \sqrt{3+4\rho^2}$	6PyI
		$\left(01\bar{1}1\right)$	$\left[-\sqrt{3}\rho, -\rho, \sqrt{3}\right] / \sqrt{3+4\rho^2}$	6PyII
		$\left(11\bar{2}2\right)$	$\left[-2\rho, 0, 2\right] / \sqrt{4+4\rho^2}$	6sP
$\boldsymbol{b}_7 = 1/3\left[\bar{1}\bar{1}2\bar{3}\right]$	$\left[1,0,-\rho\right]$	$\left(1\bar{1}00\right)$	$\left[0,0,1\right]$	7Pr
		$\left(\bar{1}011\right)$	$\left[\frac{\sqrt{3}}{2}, -\frac{1}{2}, 0\right]$	7PyI
		$\left(0\bar{1}11\right)$	$\left[\sqrt{3}\rho, \rho, \sqrt{3}\right] / \sqrt{3+4\rho^2}$	7PyII
		$\left(\bar{1}\bar{1}22\right)$	$\left[2\rho, 0, 2\right] / \sqrt{4+4\rho^2}$	7sP
$\boldsymbol{b}_8 = 1/3\left[\bar{1}2\bar{1}3\right]$	$\left[-\frac{1}{2}, -\frac{\sqrt{3}}{2}, \rho\right]$	$\left(\bar{1}010\right)$	$\left[\frac{\sqrt{3}}{2}, -\frac{1}{2}, 0\right]$	8Pr
		$\left(1\bar{1}01\right)$	$\left[0,2\rho,\sqrt{3}\right] / \sqrt{3+4\rho^2}$	8PyI
		$\left(0\bar{1}11\right)$	$\left[\sqrt{3}\rho, \rho, \sqrt{3}\right] / \sqrt{3+4\rho^2}$	8PyII
		$\left(1\bar{2}12\right)$	$\left[\rho, \sqrt{3}\rho, 2\right] / \sqrt{4+4\rho^2}$	8sP
$\boldsymbol{b}_9 = 1/3\left[\bar{1}2\bar{1}\bar{3}\right]$	$\left[-\frac{1}{2}, -\frac{\sqrt{3}}{2}, -\rho\right]$	$\left(\bar{1}101\right)$	$\left[0,-2\rho,\sqrt{3}\right] / \sqrt{3+4\rho^2}$	9Pr
		$\left(01\bar{1}1\right)$	$\left[-\sqrt{3}\rho, -\rho, \sqrt{3}\right] / \sqrt{3+4\rho^2}$	9PyI
		$\left(\bar{1}101\right)$	$\left[0,-2\rho,\sqrt{3}\right] / \sqrt{3+4\rho^2}$	9PyII
		$\left(\bar{1}2\bar{1}2\right)$	$\left[-\rho, -\sqrt{3}\rho, 2\right] / \sqrt{4+4\rho^2}$	9sP
$\boldsymbol{b}_{10} = \left[0001\right]$	$\left[0,0,\rho\right]$	$\left(01\bar{1}0\right)$	$\left[-\frac{\sqrt{3}}{2}, -\frac{1}{2}, 0\right]$	10PrI
		$\left(\bar{1}010\right)$	$\left[\frac{\sqrt{3}}{2}, -\frac{1}{2}, 0\right]$	10PrII
		$\left(1\bar{1}00\right)$	$\left[0,0,1\right]$	10PrIII

Dislocation segments can in general have an anisotropic mobility response which strongly depends on the segment's line orientation and crystal lattice structure (Hull and Bacon, 2011b; Hirth and Lothe, 1982). In principle, MD simulations can be performed to determine the dislocation mobility parameters for any dislocation orientation. However, in practice, mobility parameters are known for only a finite number of dislocation orientations. This is due to computational difficulties and relatively limited parametric studies

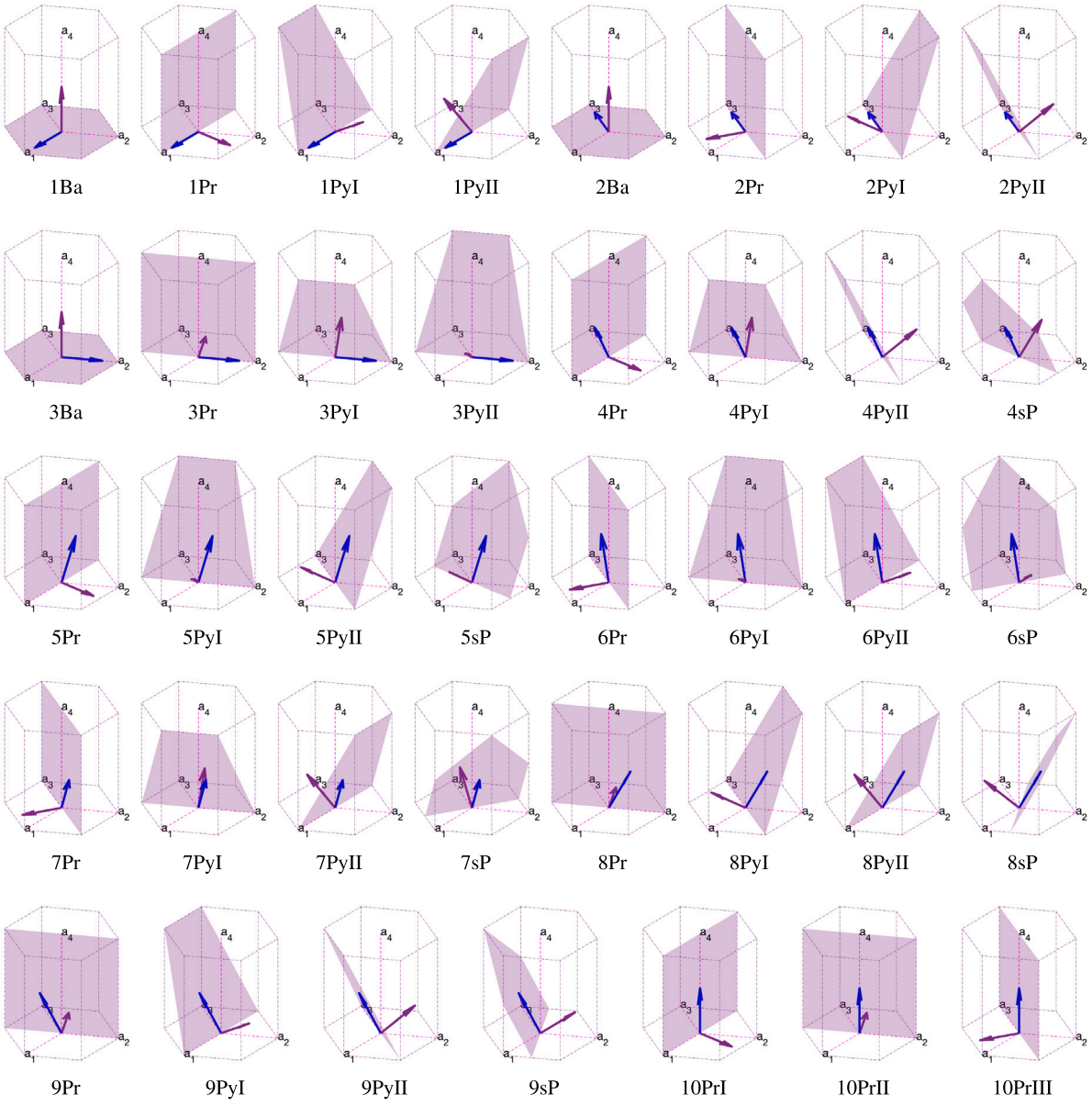


Fig. 1. Geometry of HCP slip systems including corresponding slip planes. The blue and magenta vectors are of arbitrary magnitude and respectively represent the direction of the Burgers and normal vectors. (For interpretation of the references to colour in this figure legend, the reader is referred to the web version of this article.)

available in the literature. These empirically-determined parameters must be interpolated and extrapolated in order to obtain a continuous distribution of mobility parameters so that a general dislocation orientation may be used in DD simulations.

Except for in conditions of high strain rates, dislocation inertia may be ignored due to the effects of phonon-induced drag (Hull and Bacon, 2011b). In these so-called over-damped regimes, the dislocation velocity $\boldsymbol{v}(\boldsymbol{x})$ at position $\boldsymbol{x}$ on the dislocation line can be expressed in terms of the total instantaneous driving force per unit length $\boldsymbol{f}(\boldsymbol{x})$ at that point via

$$\boldsymbol{v}(\boldsymbol{x}) = \boldsymbol{\mathcal{M}}(\boldsymbol{f}(\boldsymbol{x})) \tag{9}$$

Note that, in this context, $\boldsymbol{f}$ contains information representing all of the interactions influencing dislocation motion, including both elastic and core effects. The mobility function $\boldsymbol{\mathcal{M}}$ depends on several factors such as the material crystallography, temperature, and dislocation character angle. Although $\boldsymbol{\mathcal{M}}$ is in general a nonlinear function, linear mobility laws have been implemented for BCC (Cai and Bulatov, 2004), FCC (Arsenlis et al., 2007), and HCP (Aubry et al., 2016) crystals. Nonlinear mobility laws with closed-form expressions for $\boldsymbol{\mathcal{M}}$ have also been implemented (Po et al., 2016; Starikov and Tseplyaev, 2020).

If $\mathcal{M}$ is an injective function, then a unique inverse exists, known as the drag function $\mathcal{B}$. If $\mathcal{M}$ is a linear function, as will be assumed in this paper, then it is injective if its matrix representation can be inverted. In the over-damped regime, a dislocation drag force per unit length $\boldsymbol{f}^{\text{drag}}$ is given by

$$\boldsymbol{f}^{\text{drag}}(\boldsymbol{x}) = -\boldsymbol{\mathcal{B}}(\boldsymbol{v}(\boldsymbol{x})) \tag{10}$$

and exactly cancels the driving force per unit length $\boldsymbol{f}(\boldsymbol{x})$ at each point of the dislocation line, i.e.

$$\boldsymbol{f}^{\text{drag}}(\boldsymbol{x}) + \boldsymbol{f}(\boldsymbol{x}) = 0 \tag{11}$$

Due to the discrete nature of DD models, the velocity $\boldsymbol{v}(\boldsymbol{x})$ can only vary independently at each node, and not along segments which connect them. Therefore, we may enforce condition (11) only at the nodes. Using shape functions to account for this constraint, the velocity $\boldsymbol{v}(\boldsymbol{x})$ at an arbitrary point on a segment can be expressed as

$$\boldsymbol{v}(\boldsymbol{x}) = \sum_i \boldsymbol{v}_i \; N_i(\boldsymbol{x}) \tag{12}$$

where $\boldsymbol{v}_i$ is the velocity of node n_i and the sum is over both nodes to which the segment is connected to.

Weighing the driving force per unit length with shape functions leads to a weaker drag condition given by

$$\boldsymbol{f}_i = \oint_C N_i(\boldsymbol{x}) \; \boldsymbol{f} \; \mathrm{d}L = \oint_C N_i(\boldsymbol{x}) \; \boldsymbol{\mathcal{B}}(\boldsymbol{v}(\boldsymbol{x})) \; \mathrm{d}L \tag{13}$$

where $\boldsymbol{f}_i$ represents the driving force acting on node n_i and C represents the entire dislocation network. Since $N_i(\boldsymbol{x})$ is non-zero only along segments connected to node n_i, Eq. (13) can be expressed as

$$\boldsymbol{f}_i = \sum_j^Q \int_{\Gamma_{ij}} N_i(\boldsymbol{x}) \; \boldsymbol{\mathcal{B}}(\boldsymbol{v}(\boldsymbol{x})) \; \mathrm{d}L \tag{14}$$

where the summation is over all Q nodes n_j which are connected to node n_i. For a sufficiently finely discretised nodal network, it is reasonable and highly convenient to assume that the dislocation velocity of positions along segments are approximately equivalent to the velocity of node n_i. This results in a constant drag function $\boldsymbol{\mathcal{B}}(\boldsymbol{v}(\boldsymbol{x})) = \boldsymbol{\mathcal{B}}_{ij}(\boldsymbol{v}_i)$ along each segment, leading to

$$\boldsymbol{f}_i = \sum_j^Q \boldsymbol{\mathcal{B}}_{ij}(\boldsymbol{v}_i) \int_{\Gamma_{ij}} N_i(\boldsymbol{x}) \; \mathrm{d}L = \sum_j^Q \boldsymbol{\mathcal{B}}_{ij}(\boldsymbol{v}_i) \; \frac{1}{2} \; |\boldsymbol{L}_{ij}| \tag{15}$$

where $\boldsymbol{L}_{ij} = \boldsymbol{x}_j - \boldsymbol{x}_i$ is the segment length vector. Note that the assumption that the velocities of neighbouring nodes are approximately equivalent can be problematic in certain situations, such as at nodes connected to more than two segments with dramatically different velocities. However, this assumption should still be considered, as it greatly reduces the computational requirements of 3D DD simulations.

Furthermore, for low nodal velocities we may assume a linear mobility response, i.e. a mobility relation given by $\boldsymbol{\mathcal{B}}_{ij}(\boldsymbol{v}_i) = \mathcal{B}_{ij} \cdot \boldsymbol{v}_i$ for the drag tensor $\mathcal{B}_{ij}$ of segment Γ_{ij} (with units of Pa s). Consequently, the weak condition simplifies to become

$$\boldsymbol{f}_i = \frac{1}{2} \sum_j^Q |\boldsymbol{L}_{ij}| \; \mathcal{B}_{ij} \cdot \boldsymbol{v}_i \tag{16}$$

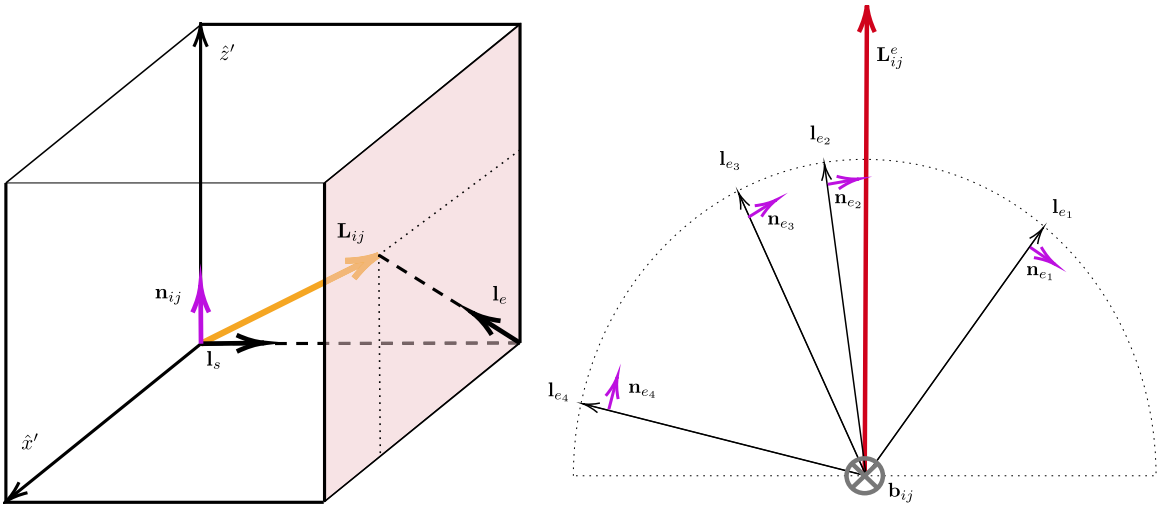
2.2.3. Drag tensor construction

The drag tensor depends on empirically-determined data which in practice is obtained for pure screw and pure edge dislocations for a limited set of glide planes. Consider a pure screw and a pure edge segment with respective drag tensors $\mathcal{B}_{ij}^{s}$ and $\mathcal{B}_{ij}^{e_q}$ with orientations on slip systems for which there exists empirical data. Suppose that, for a segment with a given Burgers vector, there are N available edge-type orientations denoted by the index q. These drag tensors may be constructed via a linear combination of rank-1 symmetric matrices expressed as

$$\begin{aligned} \mathcal{B}_{ij}^{s} &= B^{\text{line}} \boldsymbol{l}_s \otimes \boldsymbol{l}_s + B^{\text{glide}}_{\text{screw}}(\boldsymbol{b}_{ij}, \boldsymbol{n}_s) \boldsymbol{m}_s \otimes \boldsymbol{m}_s + B^{\text{climb}} \boldsymbol{n}_s \otimes \boldsymbol{n}_s \\ \mathcal{B}_{ij}^{e_q} &= B^{\text{line}} \boldsymbol{l}_{e_q} \otimes \boldsymbol{l}_{e_q} + B^{\text{glide}}_{\text{edge}}(\boldsymbol{b}_{ij}, \boldsymbol{n}_{e_q}) \boldsymbol{m}_{e_q} \otimes \boldsymbol{m}_{e_q} + B^{\text{climb}} \boldsymbol{n}_{e_q} \otimes \boldsymbol{n}_{e_q} \end{aligned} \tag{17}$$

For the following discussion, let $\boldsymbol{l}_k$, $\boldsymbol{m}_k$, $\boldsymbol{n}_k$, and $\mathcal{B}_{ij}^{k}$ respectively denote the line vector, glide vector, normal vector, and drag tensor for the corresponding segment character as expressed in Eq. (17). The drag coefficients B^{line}, $B^{\text{glide}}_{\text{screw}}$, $B^{\text{glide}}_{\text{edge}}$, and B^{climb} are the empirically-determined parameters. In principle, all of the drag coefficients could depend on the slip system of the segment, but in this model this dependency only applies to the glide drag coefficients. The fictitious drag coefficient B^{line} represents the stiffness of the nodes when moving in the line direction. This term is necessary in order to construct a full rank drag tensor. If the set $\{\boldsymbol{l}_k, \boldsymbol{m}_k, \boldsymbol{n}_k\}$ forms an orthonormal basis, the drag coefficients are the eigenvalues of the drag tensor $\mathcal{B}_{ij}^{k}$. Because the drag coefficients must be real and greater than zero to be physically meaningful, this drag tensor will always be positive-definite. If the set $\{\boldsymbol{l}_k, \boldsymbol{m}_k, \boldsymbol{n}_k\}$ is not linearly independent, the matrix $\mathcal{B}_{ij}^{k}$ is non-invertible and solving a corresponding linear system introduces singularities.

For general segment orientations, the mobility law must be capable of interpolating through all orientations for which there exists drag coefficient data. Therefore, the general drag tensor $\mathcal{B}_{ij}$ expressed in Eq. (16) will be a linear combination of tensors consisting of a form represented by Eqs. (17). For a pure screw segment, $\boldsymbol{l}_s = \hat{\boldsymbol{b}} = \frac{\boldsymbol{b}}{|\boldsymbol{b}|}$, $\boldsymbol{m}_s = \boldsymbol{l}_s \times \boldsymbol{n}_s$, and $\boldsymbol{n}_s = \boldsymbol{n}$, where the Burgers



(a) Line vector decomposition.

(b) Edge vector decomposition. Unit line vectors $\boldsymbol{l}_{e_q}$ can always be represented as lying on a half-circle without loss of generality.

Fig. 2. Segment decomposition.

vector $\boldsymbol{b}$ and normal vector $\boldsymbol{n}$ are pre-defined, i.e. they are not calculated in the mobility law from more fundamental parameters. For a pure edge segment of orientation q, $\boldsymbol{n}_{e_q} = \boldsymbol{m}_{e_q} \times \boldsymbol{l}_{e_q}$ and $\boldsymbol{m}_{e_q} = \hat{\boldsymbol{b}}$.

In this model, a segment is considered glissile if its Burgers and normal vectors are respectively parallel to a pair of Burgers and normal vectors which appear in a row of Table 1; otherwise, it is considered sessile. Consider a general, mixed-character segment Γ_{ij} with its line, Burgers, and normal vectors $\{\boldsymbol{l}_{ij}, \boldsymbol{b}_{ij}, \boldsymbol{n}_{ij}\}$ pre-defined. Suppose that $\boldsymbol{b}_{ij}$ is parallel to a Burgers vector contained in Table 1. For a glissile segment, every Burgers vector has a corresponding set of normal vectors according to this table. Let us define the map $\boldsymbol{\Phi}$ which takes a Burgers vector as input and outputs the set of corresponding normal vectors according to Table 1. Suppose that $\boldsymbol{n}_{ij}$ is parallel to a normal vector contained in $\boldsymbol{\Phi}(\boldsymbol{b}_{ij})$. The segment now fulfils the criteria required to be considered glissile. The segment length vector $\boldsymbol{L}_{ij}$ may be represented as a decomposition in terms of perpendicular pure screw and pure edge components via $\boldsymbol{L}_{ij} = L^s_{ij}\boldsymbol{l}_s + L^e_{ij}\boldsymbol{l}_e$, where $\boldsymbol{l}_s \parallel \boldsymbol{b}_{ij}$ and $\boldsymbol{l}_e \perp \boldsymbol{b}_{ij}$ are unit vectors. To study a general case, suppose that the segment is lying off-plane (see, for instance, Fig. 2(a)), i.e. $\boldsymbol{l}_{ij} \times \boldsymbol{b}_{ij}$ is not parallel to any normal vector contained in $\boldsymbol{\Phi}(\boldsymbol{b}_{ij})$ and, thus, $\boldsymbol{l}_{ij} \times \boldsymbol{b}_{ij} \nparallel \boldsymbol{n}_{ij}$. This is possible for instance in the case that node n_i experiences an asymmetric climb with respect to its connected node n_j. In such a case, the normal vector $\boldsymbol{n}_{ij}$ would still be pre-defined and should still be parallel to a normal vector contained in $\boldsymbol{\Phi}(\boldsymbol{b}_{ij})$. Since the edge component $\boldsymbol{L}^e_{ij} = L^e_{ij}\boldsymbol{l}_e$ would not lie on any plane contained in $\boldsymbol{\Phi}(\boldsymbol{b}_{ij})$, an algorithm must be devised to appropriately decompose this edge component into further edge components $L^{e_q}_{ij}\boldsymbol{l}_{e_q}$ which lie on the planes contained in $\boldsymbol{\Phi}(\boldsymbol{b}_{ij})$. The set of all unit vectors $\bigcup_q \{\boldsymbol{l}_{e_q}\}$ for which the edge component $\boldsymbol{L}^e_{ij}$ may be decomposed into is obtained via $\boldsymbol{l}_{e_q} = \hat{\boldsymbol{b}}_{ij} \times \boldsymbol{n}_{e_q}$ for all $\boldsymbol{n}_{e_q} \in \boldsymbol{\Phi}(\boldsymbol{b}_{ij})$. Note that, since the screw component $L^s_{ij}\boldsymbol{l}_s$ can always lie on any plane contained in $\boldsymbol{\Phi}(\boldsymbol{b}_{ij})$, the screw component does not need to be further decomposed.

Upon application of the chosen decomposition algorithm, the length vector for this segment may be written without loss of generality as

$$\boldsymbol{L}_{ij} = L^s_{ij}\boldsymbol{l}_s + L^{e_a}_{ij}\boldsymbol{l}_{e_a} + L^{e_b}_{ij}\boldsymbol{l}_{e_b} \tag{18}$$

The drag tensor for an arbitrary segment is then interpolated via

$$\mathcal{B}_{ij} = \frac{|L^s_{ij}|}{|\boldsymbol{L}_{ij}|}\mathcal{B}^s_{ij} + \frac{|L^{e_a}_{ij}|}{|\boldsymbol{L}_{ij}|}\mathcal{B}^{e_a}_{ij} + \frac{|L^{e_b}_{ij}|}{|\boldsymbol{L}_{ij}|}\mathcal{B}^{e_b}_{ij} \tag{19}$$

The drag tensors corresponding to the decomposition are

$$\begin{aligned}
\mathcal{B}^s_{ij} &= B^{\text{line}}\hat{\boldsymbol{b}}_{ij} \otimes \hat{\boldsymbol{b}}_{ij} + B^{\text{glide}}_{\text{screw}}(\boldsymbol{b}_{ij}, \boldsymbol{n}_{ij})\boldsymbol{m}_s \otimes \boldsymbol{m}_s + B^{\text{climb}}\boldsymbol{n}_{ij} \otimes \boldsymbol{n}_{ij} \\
\mathcal{B}^{e_a}_{ij} &= B^{\text{line}}\boldsymbol{l}_{e_a} \otimes \boldsymbol{l}_{e_a} + B^{\text{glide}}_{\text{edge}}(\boldsymbol{b}_{ij}, \boldsymbol{n}_{e_a})\hat{\boldsymbol{b}}_{ij} \otimes \hat{\boldsymbol{b}}_{ij} + B^{\text{climb}}\boldsymbol{n}_{e_a} \otimes \boldsymbol{n}_{e_a} \\
\mathcal{B}^{e_b}_{ij} &= B^{\text{line}}\boldsymbol{l}_{e_b} \otimes \boldsymbol{l}_{e_b} + B^{\text{glide}}_{\text{edge}}(\boldsymbol{b}_{ij}, \boldsymbol{n}_{e_b})\hat{\boldsymbol{b}}_{ij} \otimes \hat{\boldsymbol{b}}_{ij} + B^{\text{climb}}\boldsymbol{n}_{e_b} \otimes \boldsymbol{n}_{e_b}
\end{aligned} \tag{20}$$

where $\boldsymbol{m}_s = \boldsymbol{l}_s \times \boldsymbol{n}_{ij}$. Finally, in the case of a sessile segment, it is treated as stiff in all directions such that the drag tensor is defined as

$$\mathcal{B}_{ij} = B^{\text{line}}\boldsymbol{l}_{ij} \otimes \boldsymbol{l}_{ij} + B^{\text{glide}}_{\text{sess}}(I - \boldsymbol{l}_{ij} \otimes \boldsymbol{l}_{ij}) \tag{21}$$

where $B_{\text{sess}}^{\text{glide}}$ is the drag coefficient in all directions perpendicular to the line vector and is set to a large finite value.

As a result of the interpolation procedure, the weak condition (16) may be expressed as

$$\boldsymbol{f}_i = \frac{1}{2}\sum_j^Q \left(|L_{ij}^s|\ \mathcal{B}_{ij}^s + |L_{ij}^{e_a}|\ \mathcal{B}_{ij}^{e_a} + |L_{ij}^{e_b}|\ \mathcal{B}_{ij}^{e_b} \right) \cdot \boldsymbol{v}_i \tag{22}$$

It should be noted that the way in which the drag tensor $\mathcal{B}_{ij}$ is interpolated may result in artefacts in the segment mobility which do not reflect the physical reality. In particular, from Eq. (22), it can be seen that the drag which a given segment experiences depends on the algorithm which determines the decomposition given by Eq. (18). An ideal decomposition algorithm is one which minimises the norm of the set $\bigcup_q \{L_{ij}^{e_q}\}$, and thus minimises the effective length of the segment components which contribute to the segment drag. See Appendix A for a discussion of the decomposition algorithm.

2.2.4. Drag tensor conditioning

To determine the nodal velocities of a node connected to glissile segments, one must invert the full drag tensor given by

$$\boldsymbol{B}_i = \frac{1}{2}\sum_j^Q \left(|L_{ij}^s|\ \mathcal{B}_{ij}^s + |L_{ij}^{e_a}|\ \mathcal{B}_{ij}^{e_a} + |L_{ij}^{e_b}|\ \mathcal{B}_{ij}^{e_b} \right) \tag{23}$$

for each node of the network. Since $\boldsymbol{B}_i$ is composed of a linear combination of symmetric positive-definite matrices, $\boldsymbol{B}_i$ will also be symmetric positive-definite. Because of the large amount of times that this inversion may be performed during a simulation, it is crucial that $\boldsymbol{B}_i$ is constructed in such a way so as to not be singular or ill-conditioned.

The condition number $\kappa\left(\boldsymbol{B}_i\right)$ associated with solving for $\boldsymbol{v}_i$ in the linear system $\boldsymbol{f}_i = \boldsymbol{B}_i\boldsymbol{v}_i$ gives a measure for how sensitive the output $\boldsymbol{v}_i$ is to a change in the input $\boldsymbol{f}_i$. The condition number is roughly the factor by which any noise in the input vector $\boldsymbol{f}_i$ will be magnified when computing the solution. In the context of linear systems, $\kappa\left(\boldsymbol{B}_i\right) = \|\boldsymbol{B}_i^{-1}\|\ \|\boldsymbol{B}_i\|$ for some matrix norm $\|\cdot\|$. Using the L^2 norm, and assuming that the linear system is symmetric (such as the one in Eq. (22)), the condition number is given by $\kappa\left(\boldsymbol{B}_i\right) = |\lambda_{\max}|/|\lambda_{\min}|$, where $\lambda_{\max}$ and $\lambda_{\min}$ are respectively the maximal and minimal eigenvalues of the matrix $\boldsymbol{B}_i$. In the optimal case that the condition number is $\kappa\left(\boldsymbol{B}_i\right) = 1$, the output vector can be found with a precision which is no worse than that of the input vector. On the other hand, for finite large condition numbers, i.e. $\kappa\left(\boldsymbol{B}_i\right) \gg 1$, small errors in $\boldsymbol{f}_i$ may result in large errors in $\boldsymbol{v}_i$. The solutions of linear systems involving matrices with large condition numbers are prone to numerical error due to the amplification of errors inherent in computers using finite machine precision. When the condition number $\kappa\left(\boldsymbol{B}_i\right)$ is infinite, matrix $\boldsymbol{B}_i$ is non-invertible. Note that the maximal and minimal eigenvalues of $\boldsymbol{B}_i$ will respectively be on the order of the climb and line drag coefficients.

Because the line drag coefficient B_{ij}^{line} is not physically meaningful, it may be selected in order to optimise the stability of the mobility law. It is often set to a relatively low value to facilitate nodal distribution along segments, but not low enough such that the condition number becomes too large. Setting drag coefficients to typical values $B_{ij}^{\text{climb}} \approx 10$ and $B_{ij}^{\text{line}} \approx 10^{-5}$ yields a condition number $\kappa\left(\boldsymbol{B}_i\right) \approx 10^6$. This condition number is reasonable assuming that the error in $\boldsymbol{f}_i$ is only due to finite machine precision, i.e. it contains noise up to a factor of 10^{-16} when using double-precision floating-point arithmetic.

Even when the drag coefficients are selected with stability in mind, there may still be cases where $\kappa\left(\boldsymbol{B}_i\right)$ is very large, and other stability techniques should be considered. In the mobility law implemented in this paper, the linear system is regularised once a predetermined threshold for ill-conditioning is reached via some transformation $\boldsymbol{B}_i^{\mathcal{R}} = \mathcal{T}(\boldsymbol{B}_i)$, and the linear system $\boldsymbol{f}_i = \boldsymbol{B}_i^{\mathcal{R}}\boldsymbol{v}_i$ is instead solved. This will increase the stability of the mobility law in exchange for decreasing the accuracy of the solution. Note that calculating the L^2-based condition number of a matrix involves a costly computation of its eigenvalues. The mobility law in this paper instead uses the MATLAB function `rcond` (based on Cline et al. (1979)) which gives a more cost-efficient approximation involving the L^1-based condition number.

Given a regularisation matrix $\mathcal{R}$, the transformation

$$\boldsymbol{B}_i^{\mathcal{R}} = \boldsymbol{B}_i + \mathcal{R} \tag{24}$$

provides a simple regularisation which can be computed quickly and can induce a potentially dramatic improvement to stability. An example of a useful regularisation matrix is an isotropic noise matrix $\mathcal{R} = c\boldsymbol{I}$, where $c \geq 0$ is a regularisation parameter. This physically corresponds to an increase in the isotropic stiffness of the nodes. Another possibility is the matrix $\mathcal{R} = b\boldsymbol{l}_{ij} \otimes \boldsymbol{l}_{ij}$, where $b \geq 0$ parametrises the increase in line drag coefficient for the segments connected to the node. This will increase the minimal eigenvalue of the full drag tensor $\boldsymbol{B}_i$, and hence reduce its condition number.

A distinction is made between ill-conditioned cases, where $1 \ll \kappa\left(\boldsymbol{B}_i\right) < \infty$, and singular cases, where $\det\left(\boldsymbol{B}_i\right) = 0$ to within machine precision. In the singular case, the known components of the linear system, $\boldsymbol{B}_i$ and $\boldsymbol{f}_i$, are transformed into the eigenbasis of $\boldsymbol{B}_i$, and the dimensions corresponding to its nullspace are truncated. The solution $\boldsymbol{v}_i$ is solved for in the truncated eigenbasis, after which $\boldsymbol{v}_i$ is transformed to its original coordinate system. This is equivalent to setting node n_i to be infinitely stiff in its nullspace direction.

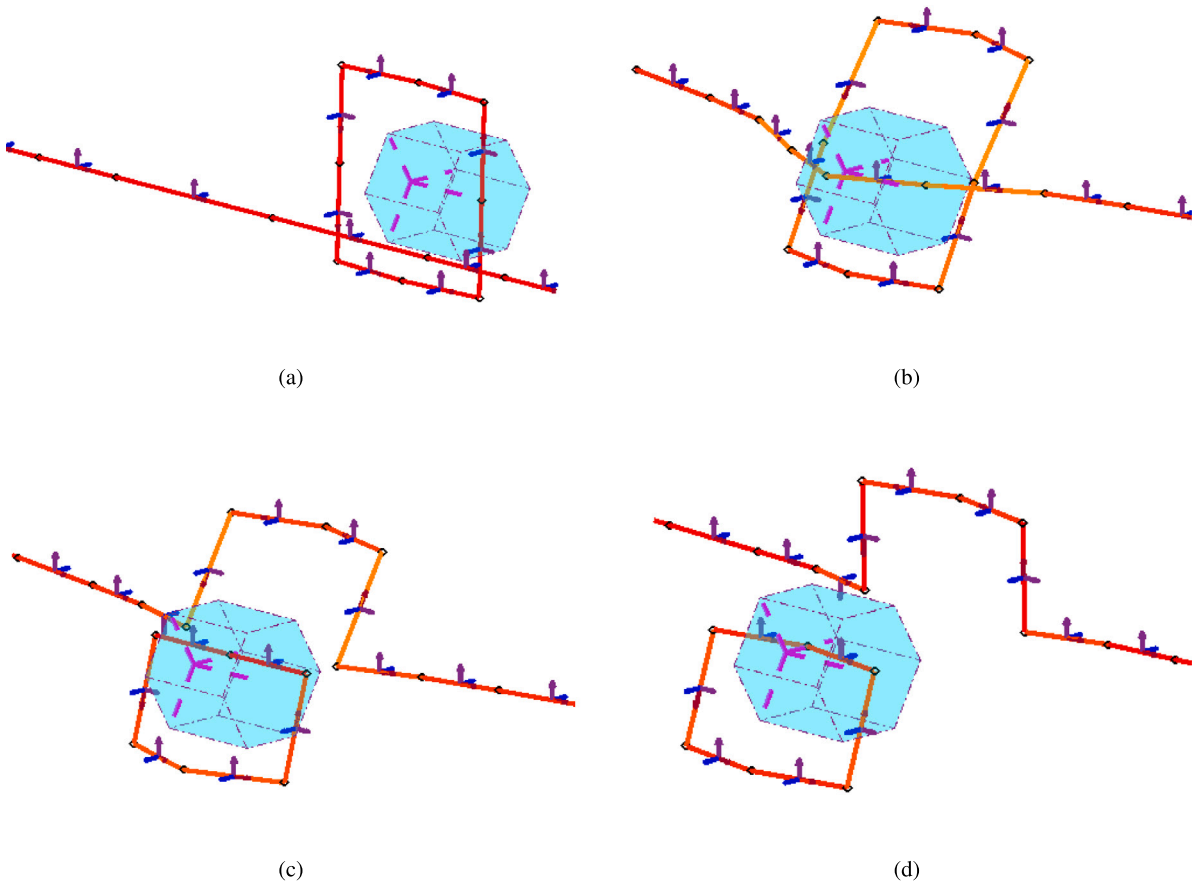


Fig. 3. Formation of a double super-jog as a result of the collision between an edge dislocation and a vacancy prismatic loop. The hexagonal prism represents the orientation of the HCP crystal axes. At the centre of each segment is a blue, magenta, and black arrow which respectively represent the segment Burgers, normal, and line vectors. The colour of segments range between red, indicating pure edge, and yellow, indicating pure screw. (For interpretation of the references to colour in this figure legend, the reader is referred to the web version of this article.)

3. 3D simulation

All 3D DD simulations were performed assuming linear isotropic elasticity and used a shear modulus of $\mu = 37.1\,\text{GPa}$, Poisson's ratio of $\nu = 0.32$ (Tarleton et al., 2015), energy density for a screw dislocation of $E_s^c = 0.125\,\text{eV}\,\text{Å}^{-1}$ (Clouet, 2012), HCP lattice parameters of $a = 3.233\,\text{Å}$ and $c = 1.593a$ (Drouet et al., 2014), and isotropic Burgers vector spreading radius of $r_c = a$. The glissile glide drag coefficients were set to $B^{\text{glide}}_{\text{screw}}(2\text{Ba}) = 180 \times 10^{-6}\,\text{Pa s}$, $B^{\text{glide}}_{\text{screw}}(2\text{Pr}) = 85 \times 10^{-6}\,\text{Pa s}$, $B^{\text{glide}}_{\text{edge}}(2\text{Ba}) = 90 \times 10^{-6}\,\text{Pa s}$, and $B^{\text{glide}}_{\text{edge}}(2\text{Pr}) = 39 \times 10^{-6}\,\text{Pa s}$ (Khater and Bacon, 2010), while the remaining drag coefficients were set to $B^{\text{line}} = 3.9 \times 10^{-6}\,\text{Pa s}$ and $B^{\text{climb}} = B^{\text{glide}}_{\text{sess}} = 10\,\text{Pa s}$. The line drag coefficient was selected such that its ratio relative to the glide drag coefficients was similar to that chosen by Aubry et al. (2016) Similarly, the climb drag coefficient was selected such that it had a similar order of magnitude to that chosen by Aubry et al. (2016).

In the 3D DD simulation an infinite domain was used. An $\langle a \rangle$-type Frank–Read source was introduced with length $L_G = 350\,\text{nm}$ of pure edge character with Burgers vector $\boldsymbol{b}_G = \frac{a}{3}[\bar{1}\bar{1}20]$ and which glides on the $(1\bar{1}00)$ prismatic plane. A square prismatic loop with Burgers vector $\boldsymbol{b}_L = -\boldsymbol{b}_G$ and side length (also referred to as a diameter) $L = 10\,\text{nm}$ is introduced $10\,\text{nm}$ ahead of the source such that its habit plane is perpendicular to the glide plane of the Frank–Read source (see Fig. 3(a)). The loop consists of four connected segments; two segments glide on the $(1\bar{1}00)$ prismatic plane while the other two segments glide on the (0001) basal plane. The line direction of a vacancy loop will correspond to the right-hand rule with respect to the Burgers vector $\boldsymbol{b}_L$; interstitial loops have an opposite line direction. Under an applied resolved shear stress τ, the edge dislocation will move towards the loop and interact with it.

Let us consider an applied resolved shear stress of $\tau = 100\,\text{MPa}$ in the $(1\bar{1}00)$ plane along the $\boldsymbol{b}_G$ direction. Let the glide plane of the edge dislocation cross the centre of the loop. The two segments of the prismatic loop gliding on the $(1\bar{1}00)$ prismatic plane will experience an induced Peach–Koehler force due to the external applied stress. Because these segments have the same Burgers vector but opposite line directions, these Peach–Koehler forces act in opposite directions, which induce a tilt in the glide cylinder

of the loop. In isolation from other dislocation structures, the loop will continue tilting until it reaches an equilibrium angle due to a combination of multiple dynamic forces acting on its segments: the longitudinal and torsional core forces, the elastic self-forces, and the long-ranged elastic forces generated by each segment.

As the edge dislocation approaches the vacancy loop, the long-ranged elastic interaction of the edge dislocation will begin to take effect. The segment of the prismatic loop which has the same Burgers vector and line direction as the edge dislocation will experience an elastic repulsive force which will also contribute to the tilting of the loop (see Fig. 3(b)). Depending on the applied resolved shear stress and the tilt of the loop, the edge dislocation will either not react with the loop due to repulsive forces, react to form a single dislocation network consisting of a junction or crossed state (Wickham et al., 1999), or react to form two distinct sets of dislocation structures (see Fig. 3(c)). If the applied resolved shear stress is insufficient, the loop will be pushed along its glide cylinder by the edge dislocation and they will not collide. Under a sufficiently great applied resolved shear stress, as is the case with $\tau = 100\,\text{MPa}$, the edge dislocation will react to form the last scenario: the outgoing structure consists of an edge dislocation with an attached double super-jog. This has been referred to as an R3 reaction by Bacon et al. (2009). What remains consists of a rectangular prismatic loop which has half of the width of the square prismatic loop (see Fig. 3(d)). As the outgoing edge dislocation continues to travel due to the applied stress, it will experience elastic and core forces due to its attached double super-jog which will result in a dragging effect, effectively reducing its mobility (see Appendix B for a discussion of this effect). Meanwhile, the remaining rectangular prismatic loop will reach a relaxation tilt angle which is dependent on the applied stress.

If an identical simulation is repeated except with an interstitial loop replacing the vacancy loop, a similar process will occur. The notable difference is that, as a result of the collision reaction, the outgoing edge dislocation will obtain an attached double-super jog which is removed from the half of the prismatic loop that is below the glide plane of the initial edge dislocation shown in Fig. 3(a) (instead of from the half of the prismatic loop above said glide plane, as is the process depicted in Fig. 3). This type of reaction will also occur if the same simulation is performed with a vacancy loop, but the edge dislocation is of opposite sign. Therefore, the position of the attached double super-jog on the outgoing edge dislocation is dependent on the relative sign of the two initial dislocation structures.

In general, if the glide plane of the edge dislocation crosses the vacancy loop and the two dislocation structures react, the part of the loop above (or, for an interstitial loop, below) said glide plane will be absorbed on the edge dislocation as a double super-jog. In addition, if the loop has some lateral tilt towards the basal plane, the edge dislocation will consecutively interact with each side of the loop one after another, resulting in a temporary single intermediary dislocation structure consisting of a helical turn along an edge dislocation.

In MD simulations of an edge dislocation interacting with an $\langle a \rangle$-type prismatic loop performed by Serra and Bacon (2013), results which match our DD simulations were reported. Of particular note, they observed the cutting and absorption of the loop by the edge dislocation via the same mechanisms as those observed in our DD simulation. They also observed the temporary single intermediary helical structure in the dislocation-loop interaction. In the case that the glide plane of the edge dislocation intersects the centre of the loop, they observed that the loop was pushed along its glide cylinder without colliding. In general, the critical stress required for edge dislocations to penetrate the loops was lower than in our DD simulations. However, it should be noted that the loops they investigated had a significantly smaller size ($L \approx 3\,\text{nm}$) than the ones investigated in our study. Regardless, the similarities found in both studies employing different length scales is a testament to the effectiveness of DD in representing small-scale interactions which are significantly impacted by inelastic effects.

In addition, Drouet et al. (2014) performed a similar DD simulation of an edge dislocation interacting with a vacancy prismatic loop with identical relevant initial conditions. The key features of their simulation results which match ours are as follows. In their simulation, the prismatic loop, initially negligibly affected by the distant edge dislocation, first rotates in its glide cylinder due to the external applied stress, eventually reaching an equilibrium tilt angle. As the edge dislocation approaches the prismatic loop due to the external applied stress, both dislocations experience a mutual repulsion. For a high enough external applied stress (in this case, it is sufficient to give a resolved shear stress of $\tau = 100\,\text{MPa}$), the dislocation collides with the loop, a double super-jog is formed on the outgoing edge dislocation in the same orientation as the one depicted in Fig. 3(c), and a prismatic loop with half of the original width is left behind. Finally, if the simulation is repeated with the loop being of interstitial type instead of vacancy type, the outgoing dislocation obtains a double super-jog on the opposite side of its glide plane relative to the one depicted in Fig. 3(c). Therefore, our simulation matches the simulation results obtained by Drouet et al. (2014), providing an independent validation of the HCP mobility law used in this paper.

From this simulation the pertinent features of the microscopic dislocation-loop interaction mechanism can be identified so that they can be implemented in a 2.5D DD model to represent coarse-grained dislocation-loop collisions. Most importantly, edge dislocations reduce the size of prismatic loops by an amount depending on the height at which they hit the loop and on the relative sign between both structures.

4. Prismatic loop dynamics and stability analysis

4.1. Segment-segment interactions

Let us consider a square prismatic vacancy loop with side length (also referred to as diameter or size) L absent of external stress fields as in Figs. 4(a) and 4(b). Because the character of the field solutions of prismatic loops with respect to the magnitude of the Burgers vector is even, the results of this section also apply equivalently for interstitial loops. The loop consists of four segments: Γ_{41}, Γ_{12}, Γ_{23}, and Γ_{34}. The elastic and core forces on each node can be calculated via Eqs. (1) and (4), respectively. Let the loop

Table 2
Stability of the elastic interaction of different sets of segments with each other in a square prismatic loop.

Elastic segment interaction	Reaction outcome
$\Gamma_{\text{tot}} \to \Gamma_{\parallel}$	Stability
$\Gamma_{\text{tot}} \to \Gamma_{\perp}$	Instability
$\Gamma_{\perp} \to \Gamma_{\parallel}$	Stability
$\Gamma_{\perp} \to \Gamma_{\perp}$	Instability
$\Gamma_{\parallel} \to \Gamma_{\parallel}$	Instability
$\Gamma_{\parallel} \to \Gamma_{\perp}$	Instability

habit plane initially lie on a 2nd order prismatic plane, and let the loop have the capacity to tilt towards the 1st order prismatic plane; ignore tilting towards the basal plane. Let this tilting process be purely conservative, i.e. let each segment be fixed to its glide plane. Assume also that the loop maintains a planar shape regardless of its tilt. The tilt angle θ is defined as the angle between the Burgers vector and habit plane normal vector of the loop. In order to investigate the angular stability of the loop, we shall analyse the total nodal forces $\boldsymbol{f}_1$ and $\boldsymbol{f}_4$ acting on nodes n_1 and n_4 as a function of the loop tilt angle θ. The average restoring force per unit length can then be calculated via $\left(\boldsymbol{f}_1(\theta) + \boldsymbol{f}_4(\theta)\right)/L$. From the symmetry of the prismatic loop we have the relation $\boldsymbol{f}_1 \cdot \boldsymbol{b} = \boldsymbol{f}_4 \cdot \boldsymbol{b} = -\boldsymbol{f}_2 \cdot \boldsymbol{b} = -\boldsymbol{f}_3 \cdot \boldsymbol{b}$. Therefore, when projected into the glide plane $\hat{\boldsymbol{m}} = -\hat{\boldsymbol{b}}$ of segment Γ_{41}, the restoring force expression becomes

$$f^{\text{R}}(\theta) = -\frac{2\boldsymbol{f}_1(\theta) \cdot \hat{\boldsymbol{b}}}{L} \tag{25}$$

It is this expression that can be used by 2D DD codes to represent the corrective restoring forces acting on prismatic loops. The restoring force arising due to elastic and core contributions will be respectively denoted as $f^{\text{R,e}}$ and $f^{\text{R,c}}$. For reference, the restoring force acting on an edge dipole (as in Fig. 4(c)) is given by

$$f^{\text{R}}_{\text{ed}}(\theta) = \frac{\mu}{2\pi(1-\nu)L} \frac{\tan\theta\,(\tan^2\theta - 1)}{(\tan^2\theta + 1)^2} \tag{26}$$

and arises only due to elastic interactions. The stable equilibrium tilt angle of an edge dipole will always be $\theta_{eq} = \pi/4$, independent of the separation distance L.

Note that for this section we define three types of equilibrium tilt angles which apply only to isolated dislocation structures without the influence of external stress: θ^{e}_{eq}, θ^{c}_{eq}, and θ_{eq}. They are respectively the equilibrium tilt angles which would be induced by the isolated elastic forces of the structure, the isolated core forces, and the combined elastic and core forces.

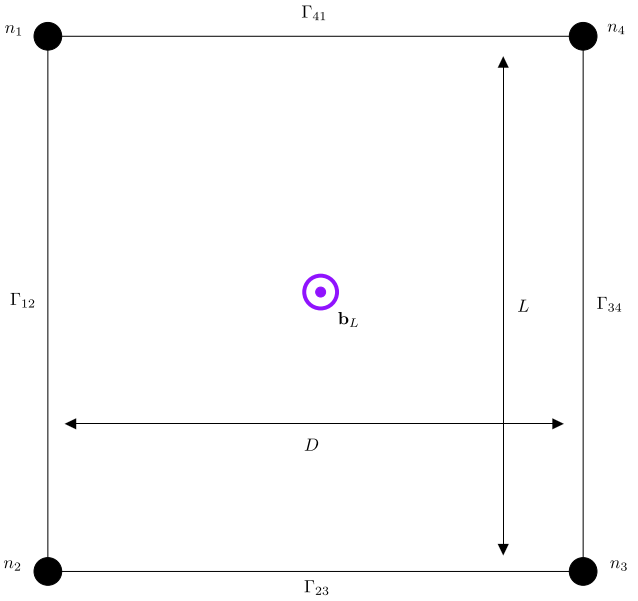
Let us now analyse the effect of each of the segments of the square prismatic loop on its stability. Motivated by the comparison to the 2D model, the four segments may be aggregated into two sets: the segments $\Gamma_{\perp} = \{\Gamma_{41}, \Gamma_{23}\}$ and the segments $\Gamma_{\parallel} = \{\Gamma_{12}, \Gamma_{34}\}$ which respectively represent the dislocations perpendicular and parallel to the plane of the 2D model. Let $\Gamma_{\text{tot}} = \Gamma_{\perp} \cup \Gamma_{\parallel}$ denote the set of all the segments. Segments $\Gamma_{\perp}$ can be partially modelled by 2D DD models, while segments $\Gamma_{\parallel}$ cannot. We may investigate the individual effects of $\Gamma_{\perp}$ and $\Gamma_{\parallel}$ by calculating $f^{R}(\theta)$ for each isolated set. The elastic nodal force on node n_1 is given by

$$\boldsymbol{f}^{\text{e}}_1 = \int_{\Gamma_{41}} N_1(\boldsymbol{x})\, \boldsymbol{f}^{\text{PK}}(\boldsymbol{x})\, \text{d}L(\boldsymbol{x}) + \int_{\Gamma_{12}} N_1(\boldsymbol{x})\, \boldsymbol{f}^{\text{PK}}(\boldsymbol{x})\, \text{d}L(\boldsymbol{x}) \tag{27}$$

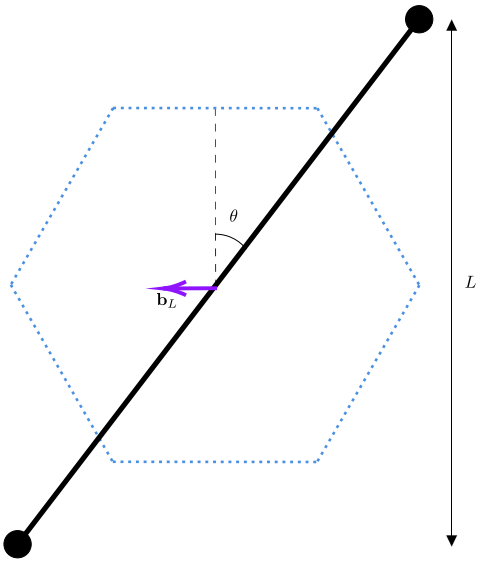
Note that the Peach–Koehler force field $\boldsymbol{f}^{\text{PK}}$ is generated by the precise structure of the entire loop. The first and second terms represent the contribution to the nodal force due to the action of the internal elastic stresses acting on the segments Γ_{41} and Γ_{12}, respectively. Due to the loop symmetry, this can be thought of as the action of the elastic restoring force on the segments $\Gamma_{\perp}$ and $\Gamma_{\parallel}$, respectively, up to a simple linear transformation given by Eq. (25). Let us denote these terms as $\boldsymbol{f}^{\text{e}}_{\text{tot}\to\perp}$ and $\boldsymbol{f}^{\text{e}}_{\text{tot}\to\parallel}$, respectively. The notation $G_{A\to B}$ can be understood as denoting the action on the set Γ_B due to the fields G arising from the set Γ_A. The elastic nodal force due to the total loop Γ_{tot} is given by $\boldsymbol{f}^{\text{e}}_{\text{tot}\to\perp} + \boldsymbol{f}^{\text{e}}_{\text{tot}\to\parallel}$.

Consider first the dynamics caused by the elastic interactions. Fig. 5(a) displays plots of the elastic restoring forces arising from and acting on the different segments of a loop of side length $L = 10\,\text{nm}$. Fig. 5(b) displays plots of the elastic restoring forces arising from full loops of varying side lengths acting on $\Gamma_{\perp}$ and $\Gamma_{\parallel}$. Let us consider the elastic fields arising due to the full loop Γ_{tot}. In this case, the fields $\boldsymbol{f}^{\text{R,e}}_{\text{tot}\to\parallel}$ that act upon $\Gamma_{\parallel}$ induce loop stability, while the fields $\boldsymbol{f}^{\text{R,e}}_{\text{tot}\to\perp}$ that act upon $\Gamma_{\perp}$ induce loop instability. Next, consider the elastic fields arising due to segments $\Gamma_{\perp}$: the fields $\boldsymbol{f}^{\text{R,e}}_{\perp\to\parallel}$ will induce loop stability in the $\Gamma_{\parallel}$ segments and the fields $\boldsymbol{f}^{\text{R,e}}_{\perp\to\perp}$ will induce loop instability in the $\Gamma_{\perp}$ segments (i.e. in themselves). Finally, consider the elastic fields arising due to segments $\Gamma_{\parallel}$: both the fields $\boldsymbol{f}^{\text{R,e}}_{\parallel\to\parallel}$ and $\boldsymbol{f}^{\text{R,e}}_{\parallel\to\perp}$ will induce loop instability in the $\Gamma_{\parallel}$ and $\Gamma_{\perp}$ segments, respectively. This information is summarised in Table 2. In general, when only considering elastic effects, the loop stability is a consequence of a competing effect between segments $\Gamma_{\perp}$ and $\Gamma_{\parallel}$. The stabilising effect and reduction of the elastic stable equilibrium angle θ^{e}_{eq} arises mostly due to the stress fields which act upon segments $\Gamma_{\parallel}$. Therefore, the source of the stabilising effect cannot be properly captured by the 2D DD framework; an extension provided by a 3D theory of elasticity is required.

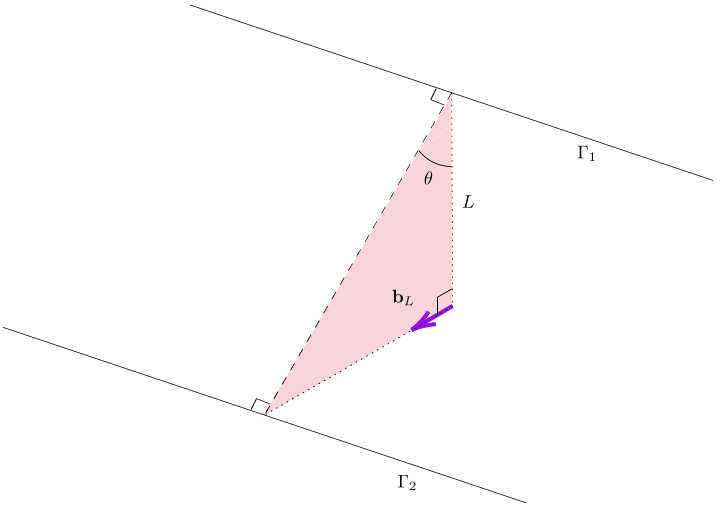
A stability analysis can also be applied to a double super-jog which is acquired by the edge dislocation. Fig. 6 shows the elastic restoring force acting on segment Γ_{41} of the double super-jog (see Fig. B.14(b)) which is created after a dislocation-loop interaction for different loop sizes. It can be shown (see Appendix B) that the structure will tend towards a stable equilibrium angle



(a) Prismatic loop in a $\theta = 0$ configuration. An initially square prismatic loop is always assumed in this paper, i.e. $D = L$.



(b) Prismatic loop in a tilted configuration. The hexagonal prism represents the crystal axes, and represents a subset of the plane which would correspond to that of a 2D DD simulation.



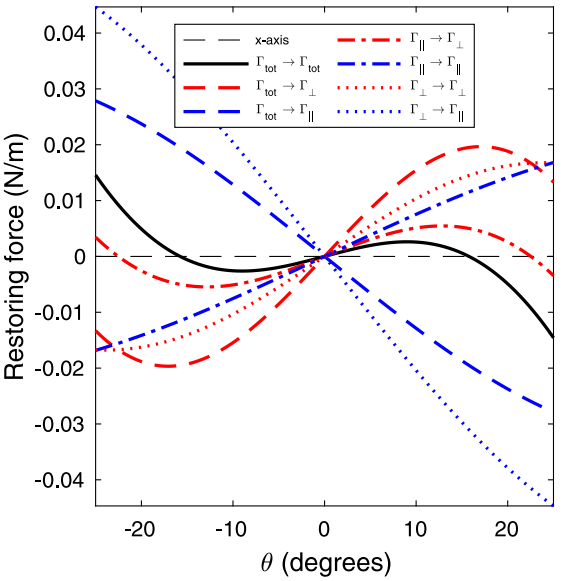
(c) Edge dipole in a tilted configuration. Segments Γ_1 and Γ_2 extend off to infinity. The red triangle represents a subset of the plane which would correspond to that of a 2D DD simulation. This dislocation structure can be understood to be the 2D approximation to the 3D prismatic loop case.

Fig. 4. Diagrams of a prismatic loop and an edge dipole.

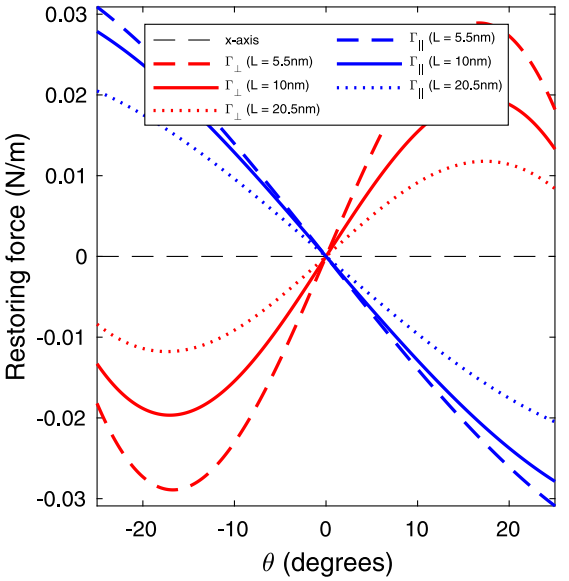
of $\theta_{eq} = 0$ in the absence of external forces. This contributes to the observed dragging effect which double super-jogs impart upon edge dislocations that they are attached to, which has been reported in the literature (Drouet et al., 2014).

4.2. Core restoring force

Let us now analyse the contribution of the core restoring force to the stability of a prismatic loop and double super-jog. Consider the core force acting on node n_1 of Fig. 4(a), projected into its glide cylinder $\hat{\boldsymbol{m}} = -\boldsymbol{b}_L$. Since this expression arises from Eq. (4), it consists of a superposition of a longitudinal component, which acts to shorten segments, and a torsional component, which acts to



(a) Elastic restoring forces arising from and acting on the different segments of a loop of side length $L = 10$ nm.



(b) Elastic restoring forces arising from loops of varying side lengths L, acting on the segments $\Gamma_{\perp}$ and $\Gamma_{\parallel}$.

Fig. 5. Plots of elastic restoring forces acting on a square prismatic vacancy loop.

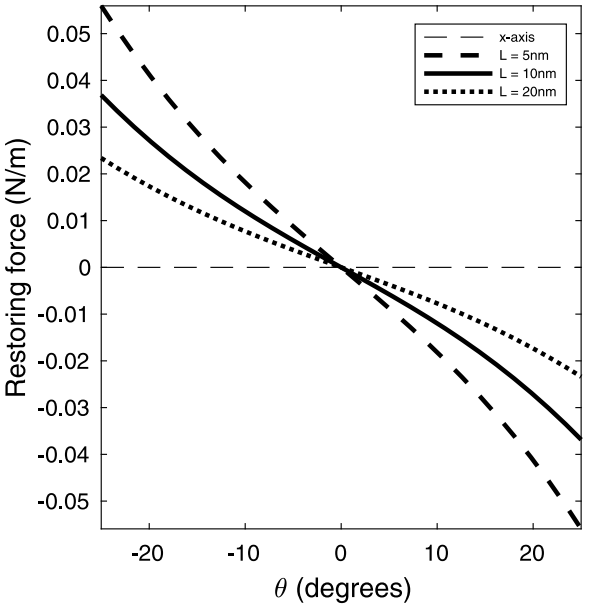


Fig. 6. Elastic restoring force on double super-jogs of varying sizes.

rotate segments into screw orientations. Because this study does not consider lateral habit plane rotations into the basal plane, and because segment Γ_{41} never changes length, the core force on n_1 will only depend on the dynamics of segment Γ_{12}. This projected core force on node n_1 is plotted in Fig. 7. As the loop begins to rotate from its pure edge configuration, the longitudinal component will always act to stabilise the extending segments and the torsional component will act to destabilise them.

The core restoring force has a simple analytical expression which can be obtained starting from Eqs. (4) and (5), given by

$$f^{\mathrm{R,c}}(\theta, L) = \frac{2}{L}\frac{E_s^c}{1-\nu}\left((2\nu - 1)\sin\theta - \nu\sin^3\theta\right) \tag{28}$$

This expression is plotted in Fig. 8(a). From the geometry of the problem, it is evident that the core contribution acts to stabilise the structure. Changing the parameters L and E_s^c will only change the magnitude of the stabilising effect. Note that, since the

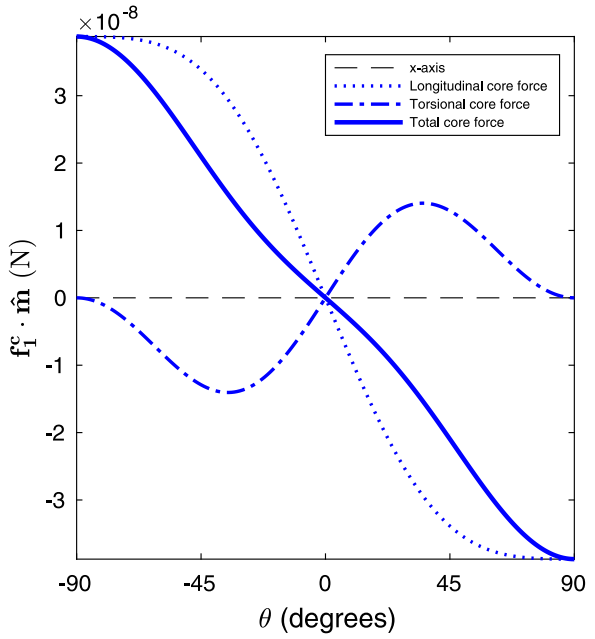
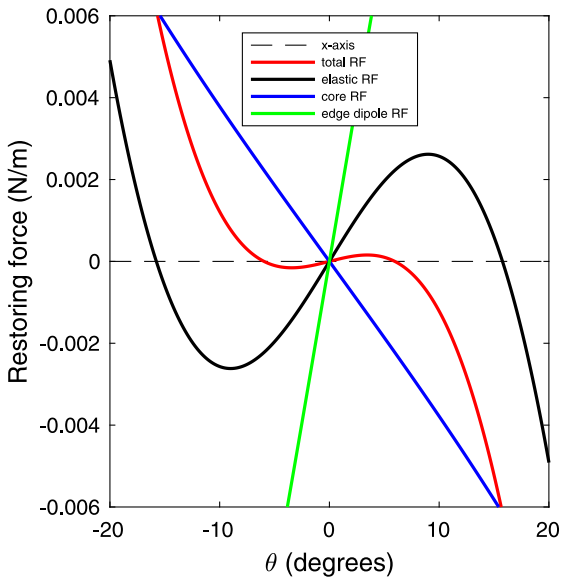
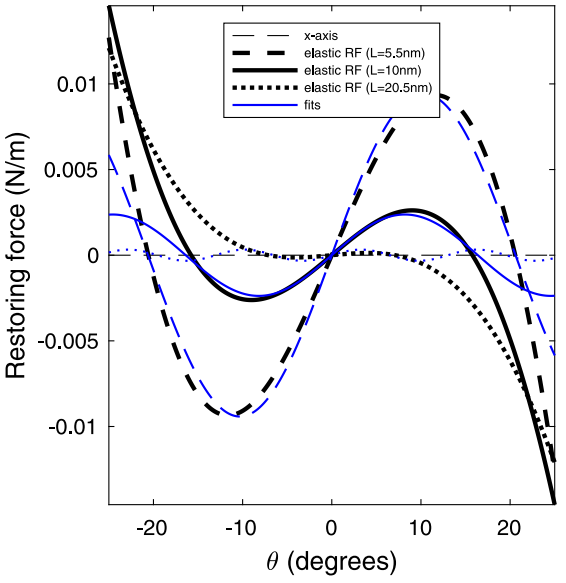


Fig. 7. Core force acting on node n_1 of the prismatic loop from Fig. 4(a), projected into its glide cylinder $\hat{\boldsymbol{m}} = -\boldsymbol{b}_L$, as a function of loop tilt angle.



(a) Restoring forces (RFs) for a vacancy prismatic loop with $L = 10$ nm. The total restoring force is the sum of the elastic and core restoring forces. The restoring force of an edge dipole of the same size is plotted for comparison.



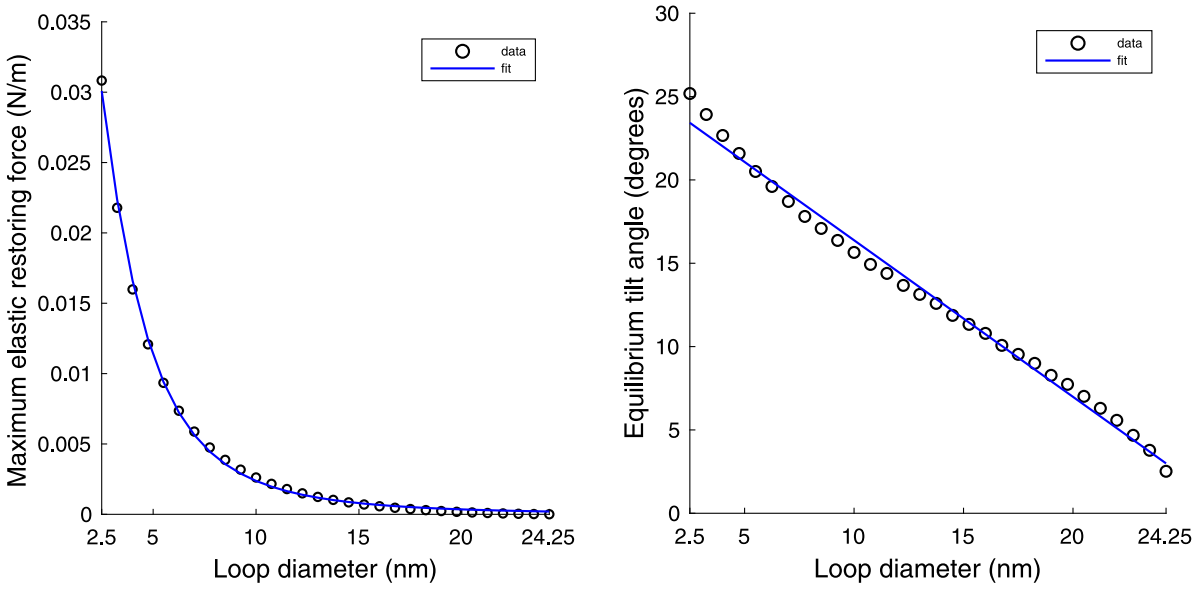
(b) Elastic restoring forces for loops of different sizes with corresponding fits. Blue curves of any pattern represent the plotted fits.

Fig. 8. Plots containing restoring forces.

only contribution to the core force on nodes n_1 and n_4 respectively come from segments Γ_{21} and Γ_{34}, the contributions to the core restoring force acting on segment Γ_{41} is the same for both the prismatic loop and double super-jog. Therefore, in this simplified representation, the core restoring force will also always act to stabilise double super-jogs.

4.3. Elastic restoring force

An analytical expression for the force exerted by a finite dislocation segment on the end node of a different finite dislocation segment with an arbitrary relative orientation has been derived and is given by Arsenlis et al. (2007). From this expression, it is



(a) Values of f_m for different loop diameters L.

(b) Values of θ^e_{eq} for different loop diameters L.

Fig. 9. Plots containing numerically-obtained data points with corresponding curves of best fit for loop sizes of $L = 2.5\,\text{nm}$ to $L = 24.25\,\text{nm}$. Only elastic interactions were considered for these plots.

possible to derive an exact analytical expression for $f^{\text{R,e}}(\theta, L)$ using the method outlined in Section 4.1. However, such an expression is complicated and contains many terms, making it unwieldy for computational implementation. Therefore, in this section, a fitting procedure will be applied to data which has been collected via numerically computing line integrals of the type shown in Eq. (27). On the other hand, the core restoring force has a simple analytical expression which does not require a fitting procedure.

Our aim now is to obtain a simple analytical expression for $f^{\text{R,e}}(\theta, L)$ which approximates the full complicated expression. In the following discussion, let us consider only elastic interactions. Elastic restoring forces are numerically computed and shown in Fig. 8(b) for loops of different sizes. From these curves, θ^e_{eq} can be found by calculating their roots. These calculated roots were found to match the values of θ^e_{eq} obtained from performing direct 3D DD simulations. In general, as L increases, θ^e_{eq} decreases, and $f_m = \sup\{|f^{\text{R,e}}(\theta, L)| : -\theta^e_{eq} \leq \theta \leq \theta^e_{eq}\}$, the maximum magnitude of the amplitude of the elastic restoring force between the range $\theta \in [-\theta^e_{eq}, \theta^e_{eq}]$, also decreases. From this observation, and from looking at the behaviour of the elastic restoring force curves, we may deduce a local expression for the elastic restoring force given by

$$f^{\text{R,e}}(\theta, L) = f_m(L) \sin\left(\frac{\pi}{\theta^e_{eq}(L)}\theta\right) \tag{29}$$

with a range of validity $\theta \in [-\theta^e_{eq}, \theta^e_{eq}]$. Since θ^e_{eq} is a stability point, this range of validity will represent many physical configurations of the prismatic loop found in simulations.

Values of $f_m(L)$ and $\theta^e_{eq}(L)$ were numerically computed for a range of loop sizes and are respectively shown in Figs. 9(a) and 9(b). It is evident that $\theta^e_{eq}(L)$ may be approximated as a linear function. Several candidate functions exist to fit the maximum amplitude $f_m(L)$; taking inspiration from standard forms for non-singular field expressions, the chosen fits were given by

$$f_m(L) = \sigma_0 \frac{\beta}{(L^\upsilon + \alpha^\upsilon)^\upsilon}, \qquad \theta^e_{eq}(L) = c_1 L + c_2 \tag{30}$$

where β, α, υ, c_1, and c_2 are fitting parameters. Note that $\sigma_0 = \mu/(2\pi(1-\nu))$ is not a fitting parameter, but rather a pre-factor that is the same as that found in typical elastic field expressions. The fitting parameters for $f_m(L)$ were obtained by solving a nonlinear least squares system via Gauss–Newton iteration. Note that a unique global minimum for β, α, and υ was not found. The fitting parameters for θ^e_{eq} were obtained via simple linear regression. The corresponding fits for $f_m(L)$ and $\theta^e_{eq}(L)$ are superimposed on Fig. 9. The values and units of the five fitting parameters are given in Table 3. These fits were obtained from a data set consisting of loop sizes ranging from $L = 2.5\,\text{nm}$ to $L = 24.25\,\text{nm}$; greater loop sizes all had values of zero for θ^e_{eq}.

Table 3
Fitting parameter values and units for the elastic restoring force shown in Eqs. (30).

Fitting parameter	Value
β	$1.1741 \times 10^{-37} \cdot \mathrm{m}^{\upsilon^2+1}$
α	$3.8796 \times 10^{-9} \cdot \mathrm{m}$
υ	7/4 (unitless)
c_1	$-1.6397 \times 10^{7} \cdot \mathrm{m}^{-1}$
c_2	0.4499 (unitless)

4.4. Total restoring force

We must now combine the core and elastic restoring forces to create a total restoring force expression which reflects the limited range of validity of the elastic component. One may use the piecewise expression given by

$$f^{\mathrm{R}}(\theta, L) = \begin{cases} f^{\mathrm{R,c}}(\theta, L) + f^{\mathrm{R,e}}(\theta, L) & |\theta| \leq \theta^{e}_{eq} \\ f^{\mathrm{R,c}}(\theta, L) & |\theta| > \theta^{e}_{eq} \end{cases} \tag{31}$$

where θ^{e}_{eq} is the equilibrium tilt angle of an isolated square prismatic loop which only endures elastic interactions. When large external stresses result in $\theta \gg \theta^{e}_{eq}$, Eq. (31) fails in supplying the sufficient restoring action to produce a realistic equilibrium tilt angle. In such a case, one possible correction to Eq. (31) and to the loop dynamics is to set the loop to be infinitely stiff with respect to external stresses which tend to increase its tilt angle outside of the range of validity $\theta \in [-\theta^{e}_{eq}, \theta^{e}_{eq}]$. This prevents the prismatic loop from obtaining values of θ outside of the range of validity. Note that as the loop size increases, this method yields increasingly spurious results, since large prismatic loops will effectively lose most or all of their tilting capability. Alternatively, values for the total restoring force over the entire range of tilt angles from $-90°$ to $90°$ can be numerically computed and interpolated to provide the full behaviour if necessary, e.g. for 2.5D DDP codes.

5. Investigations by 2.5D DDP model

The DDP code used in this section is a further enhancement of the one previously developed by Tarleton et al. (2015), which uses the formulations established by Lubarda et al. (1993) and Giessen and Needleman (1995). In the present DDP model, $\langle a \rangle$-type prismatic loops are idealised in the same way as described in previous sections of this paper. The loop segments that intersect the simulation plane (see Fig. 4(c)) are represented as edge dipoles in either interstitial or vacancy orientations, i.e. with extra half planes aligned and either pointing towards or away from one another. To inform the planar model with the essential three-dimensional information that captures the effect of all loop segments on loop tilting, f^{R} is incorporated as an additional force acting on the dipole of edge dislocations that represent the prismatic loop in the simulation plane, hence making the planar DDP model 2.5D in character. However, the DDP model requires f^{R} to be evaluated for the full range of possible tilt angles, i.e. from $-90°$ to $90°$. Since the restoring force for a particular loop size already includes the effect of the elastic stress fields of the full square prismatic loop, the elastic interaction between the dipole of edge dislocations representing the prismatic loop in the planar DDP model is omitted from the computation to avoid double counting. For all of the simulations in this section, the elastic restoring force was numerically computed at 1000 points in the range $-90°$ to $90°$ from the non-singular elastic stress expressions given in Cai et al. (2006), which was then added to the analytical core restoring force expression to obtain an angular discretisation of the total restoring force for all loop sizes simulated. These values were then interpolated to capture the restoring force for all possible tilt angles θ. Numerically computed total restoring force curves over the full range of tilt angles and for various loop sizes are shown in Fig. 10. The restoring force was added to the Peach–Koehler force $\boldsymbol{f}^{\mathrm{PK}}$ to calculate the velocity of the loop dislocations, υ_{loop}, according to:

$$\upsilon_{\mathrm{loop}} = \frac{f^{\mathrm{PK}} + f^{\mathrm{R}}(\theta, L)}{\mathrm{B}_{\mathrm{drag}}} \tag{32}$$

where the drag coefficient $\mathrm{B}_{\mathrm{drag}}$ is assigned a typical value of 4×10^{-4} Pa s.

5.1. Loop stability analysis

To validate the 2.5D implementation and investigate the stability of prismatic loops for a range of loop sizes and applied strains, a simple uniaxial tension boundary value problem was used, as shown in the schematic of Fig. 11(a). The simulation box contains only one prismatic slip system oriented $45°$ to the horizontal direction, which passes through the centre of the simulation box, and a single prismatic vacancy loop with its habit plane initially perpendicular to the slip direction. In this section, the loop size L is assumed to remain constant during a given simulation and is unaffected by the tilting. A simulation box large enough such that loop dislocations do not interact with the free surfaces was used in the simulations to mimic the situation in the three-dimensional dislocation dynamics model. In an infinite half plane, infinitely-long straight-line edge dislocations oriented as in Fig. 11(a) (i.e. an infinitely deep loop with elastic interactions but without the effect of core interactions) would tilt to an equilibrium angle of $45°$. To determine an appropriate box size, the simulation box was maintained at a 3:1 aspect ratio and increased in size until a stable

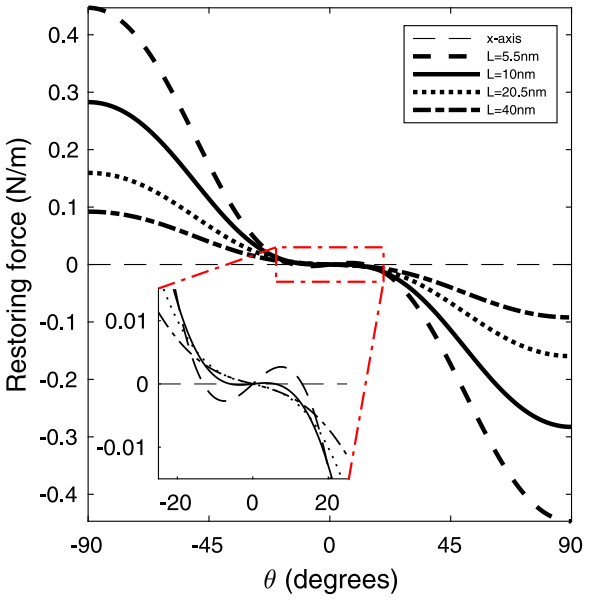


Fig. 10. Plot containing numerically computed total restoring force curves for various loop sizes.

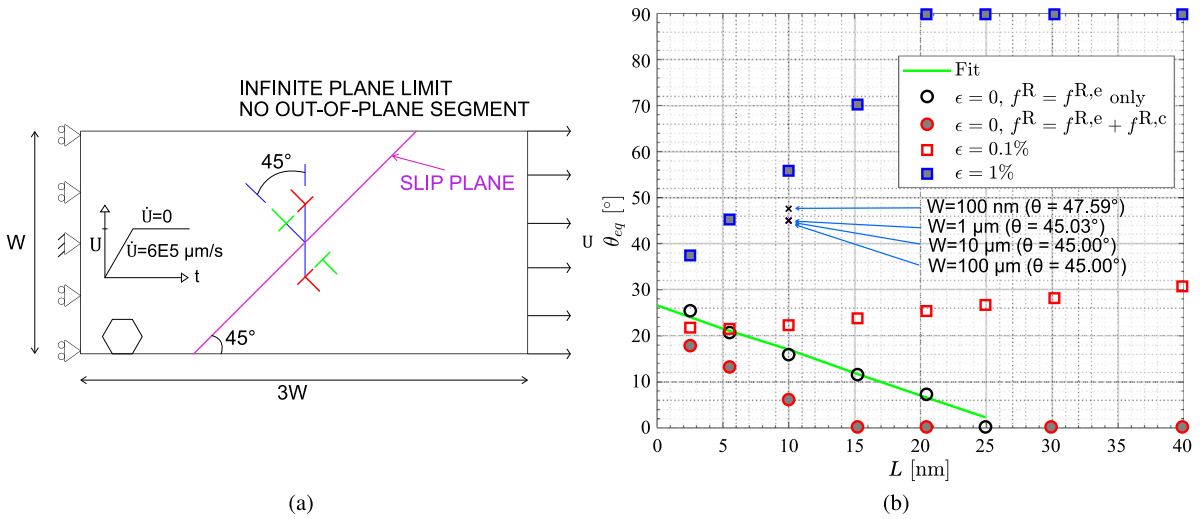


Fig. 11. (a) A boundary value problem depicting a one loop – one slip system problem in a simulation box of size of $300 \times 100\,\mu m^2$. The vacancy loop shown as an edge dipole in climb configuration tilts by 45° degrees after the initial position (represented in green) of the loop is perturbed (represented in red). (b) DDP simulations are performed to understand the effect of loop size L on the evolution of equilibrium tilt angle θ_{eq} for one unstrained and two strained configurations. The unstrained θ_{eq} values match the values in Fig. 9(b). The fit line for $\theta^{e}_{eq}(L)$ depicted in Fig. 9(b) is also plotted in green for reference. The simulation box size effect on the equilibrium angles of an edge dipole of size $L = 10\,nm$ is also shown; the smallest simulation box (W = 100 nm) generates the highest boundary stresses that prompt the edge dipole to adopt an equilibrium angle furthest away from the 45° angular position. (For interpretation of the references to colour in this figure legend, the reader is referred to the web version of this article.)

45° was achieved for a loop with $L = 10\,nm$, as shown in Fig. 11(b). The smallest box size (W = 100 nm) provides the highest instability to the equilibrium position ($\theta_{eq} = 47.59°$); a simulation box with size W = 100 μm was found to be more than sufficient ($\theta_{eq} = 45.000°$) to ensure that the loop dislocations were devoid of free surface interactions.

Simulations were performed using the 2.5D model to investigate the equilibrium tilt angles θ_{eq} under the action of the restoring force and applied loading for various loop sizes (ranging from $L = 2.5\,nm$ to $L = 40\,nm$) of $\langle a \rangle$-type prismatic loops in both unstrained and strained samples. In the zero applied strain simulations, the system is allowed to equilibrate until loop tilting terminates (i.e. until $v_{loop} < 1 \times 10^{-9}\,m\,s^{-1}$); this is a quasi-equilibrium state with respect to the timescale of the simulation. A constant time step of $\Delta t = 5 \times 10^{-10}\,s$ is generally used for the simulations but, due to the higher nonlinearity of the $f^{R}(\theta, L)$ versus θ curves shown in Fig. 10 for smaller loop sizes, a smaller time step is also selected in some cases. The open black circles on Fig. 11(b) depict the

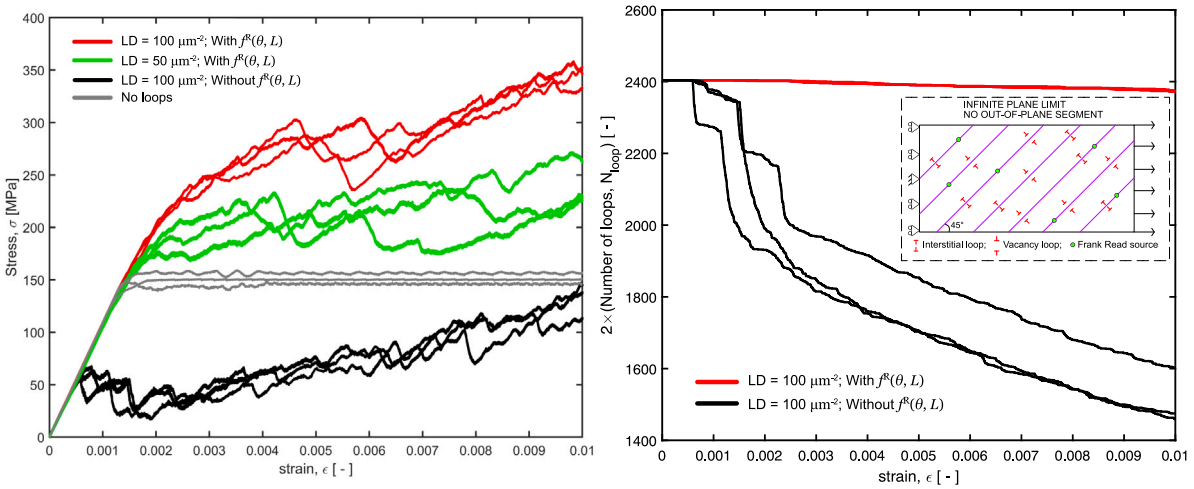


Fig. 12. (a) The effect of restoring force $f^{\mathrm{R}}(\theta, L)$, with or without, on the evolution of flow stress for a loop density of $100\,\mu\mathrm{m}^{-2}$ in the DDP model. A case with a loop density of $50\,\mu\mathrm{m}^{-2}$ that considers the $f^{\mathrm{R}}(\theta, L)$ effect and a reference simulation without loops is also shown. (b) The effect of $f^{\mathrm{R}}(\theta, L)$ on the escape of loop dislocations from the sample surface. An inset shows a schematic of the boundary value problem used in the simulations. (For interpretation of the references to colour in this figure legend, the reader is referred to the web version of this article.)

equilibrium tilt angles of loop dislocations as a function of loop size when only considering the effect of the elastic restoring force (i.e. ignoring core effects). The equilibrium tilt angles calculated using the 2.5D model exactly match the ones obtained in Fig. 9(b), which validates the 2.5D implementation. The fitting model presented in Eq. (29) is also shown for reference as a green line, which is the same as the line of fit presented in Fig. 9(b). The effect of the total restoring force $f^{\mathrm{R}}(\theta, L)$, including both $f^{\mathrm{R,e}}(\theta, L)$ and $f^{\mathrm{R,c}}(\theta, L)$, is depicted by the red filled circles in Fig. 11(b) for the zero applied strain case, where it is observed that the equilibrium tilt angle decreases with an increase in loop size. Specifically, the $\langle a \rangle$-type prismatic loops with $L > 12\,\mathrm{nm}$ are observed to show no tilting and are stable at zero degrees. Although the full 3D situation is more complex, the trend that sufficiently large loops do not tilt (with respect to the timescale of the simulation) under zero applied strain is primarily a result of the weaker elastic interaction of the perpendicular loop segments for larger loop sizes (i.e. as those segments become further apart).

Further simulations were performed to investigate the effect of applied strain on the stable equilibrium tilt angles of $\langle a \rangle$-type prismatic loops as a function of loop size. Plot points corresponding to strain values of $\epsilon = 0.1\%$ and $\epsilon = 1\%$ are depicted by the red empty squares and blue filled squares, respectively, in Fig. 11(b). The displacement rate is set to $\dot{\mathrm{U}} = 6 \times 10^5\,\mu\mathrm{m\,s}^{-1}$ to achieve a strain rate of $\dot{\epsilon} = 2000\,\mathrm{s}^{-1}$ for these simulations. After the completion of the loading step, the loops are allowed to equilibrate further with $\dot{\mathrm{U}} = 0\,\mu\mathrm{m\,s}^{-1}$, as shown in the schematic inset in Fig. 11(a), until $v_{\mathrm{loop}} < 1 \times 10^{-9}\,\mathrm{m\,s}^{-1}$. In both strained cases, smaller loops are observed to have smaller equilibrium tilt angles compared to larger loops, which may indicate a higher resistance to certain types of deformation, e.g. a dislocation acting to drive a loop to a greater tilt angle will encounter greater resistance from a smaller loop, which in turn may have implications for the mechanics of irradiation hardening; this effect is due to the greater magnitude of the restoring force for smaller loops at larger angles (see Fig. 10), or more specifically, at angles considerably larger than the zero-strain equilibrium tilt angle for the smallest loop in the comparison. Moreover, in the $\epsilon = 1\%$ case the larger loops with $L > 15\,\mathrm{nm}$ show little resistance to the deformation and equilibrate at angles approaching 90°.

5.2. Restoring force and loop density effects on flow stress

In order to demonstrate the importance of $f^{\mathrm{R}}(\theta, L)$ on the mobility of loop dislocations and the overall deformation behaviour via Eq. (32), the boundary value problem shown in the inset of Fig. 12(b) is simulated using the 2.5D DDP code with multiple loops present. Virtual samples are $6\,\mu\mathrm{m} \times 2\,\mu\mathrm{m}$ in size, and a single slip (planes at 45°) situation without obstacles is chosen to elucidate the effect of $f^{\mathrm{R}}(\theta, L)$. The slip plane spacing is taken to be $100b$, and there are a total of 170 slip planes in the sample. Frank–Read sources are randomly distributed on the slip planes with a density of $5\,\mu\mathrm{m}^{-2}$. Their strength is taken from a Gaussian distribution with mean source strength 110 MPa and standard deviation 20 MPa. The loop sizes are also taken from a distribution with mean 10 nm and standard deviation 0.1 nm. Loops are distributed randomly, but are centred about slip planes, and the total mass of loops is conserved (implying equal total vacancy and interstitial loop lengths). The dislocation-loop interaction is similar to the mechanism explained in Section 3, whereby a loop may be cut by a dislocation nucleated from a Frank–Read source upon contact, but is restricted to a discretised reduction process that on average resolves the statistics of dislocation-loop interactions over the sample: a loop is initially at full length, is then cut to half its length, and is then reduced to zero length. Slip is not generated by loop dislocations until they move.

Two loop density cases of $50\,\mu m^{-2}$ and $100\,\mu m^{-2}$ were simulated, along with a reference simulation with no loops, for three realisations (same set of input parameters) each to capture the statistical scatter (see Fig. 12(a)). In the reference case (light black curves), it is evident that the flow stress is consistent with that required to activate dislocation sources on 45° planes with an average 110 MPa strength, with no apparent source of significant strengthening in this single-slip, no-obstacle, no-loop model setup. In the cases when loops and $f^{R}(\theta, L)$ are included, there is a significant increase in flow stress observed relative to the reference case that increases with increasing loop density, as shown by the green and red curves, respectively, in Fig. 12(a). This trend is in agreement with the general observation in the literature that correlates greater loop density with greater irradiation hardening, and also demonstrates the significant role of $f^{R}(\theta, L)$ in the 2.5D DDP model, even for this very simple case. In the simulations with $100\,\mu m^{-2}$ loop density without $f^{R}(\theta, L)$ included (dark black curves), in which loop dislocations are in effect edge dislocations interacting only with each other, the other dislocations in the system, and the boundary conditions, the flow stress is markedly lower compared to the case with no loops at all. The mechanism is that loops restrained from tilting by $f^{R}(\theta, L)$ are able to remain in the system, are relatively difficult to tilt beyond their no-strain equilibrium angle, and therefore block slip from Frank–Read dislocations which elevates the flow stress, especially for higher loops densities; whereas when $f^{R}(\theta, L)$ is not included, the two dislocations making a loop are free to glide away from each other easily, particularly as straining occurs and other dislocations are nucleated, which together imbalances the pair further. This, in turn, enhances slip, allowing the material to deform plastically at a lower flow stress compared to no loops at all. The mechanism is corroborated by the number of loop dislocations plotted against strain as shown in Fig. 12(b). A very small, gradual decrease in loop dislocations is observed when $f^{R}(\theta, L)$ is included (red curves), which indicates the restraining effect on loop dislocations of the out-of-plane segments captured by $f^{R}(\theta, L)$; very few loop dislocations are able to escape at the free surfaces during the straining. This is in stark contrast to the case without $f^{R}(\theta, L)$, in which a rapid decrease in loop dislocations is observed, particularly for lower strain values corresponding to a lower flow stress, which then stabilises but continues throughout the straining; the number of loop dislocations is reduced by roughly a third at 1% strain.

6. Summary and conclusions

The dynamics of idealised conservative square $\langle a \rangle$-type prismatic loops and double super-jogs under different conditions have been analysed. First, the reaction outcome between a vacancy/interstitial loop and an edge dislocation is simulated using the 3D DD code, EasyDD, from which a course-grained microscopic interaction mechanism has been identified for use in 2.5D DD codes. This 3D simulation incorporates a HCP mobility law, which has been elucidated in detail in this paper. Second, the angular stability and restoring force of prismatic loops of various sizes is determined through analytical and numerical calculations using the theory of linear isotropic elasticity. In addition, a mechanistic explanation for the dragging effect observed in double super-jogs is proposed. Third, 2.5D DDP analyses of the stability of prismatic loops of differing sizes in samples strained to varying amounts have been performed. In these 2.5D simulations, prismatic loops are represented by edge dipoles in climb configurations in which the effect of one dislocation on the other is replaced by the numerically calculated 3D restoring force to emulate realistic prismatic loop rotation physics.

In the 2.5D DDP analyses, it has been observed that the equilibrium tilt angle of smaller loops is less sensitive to external loading than that of larger loops, which may point to a mechanistic effect of loop size on irradiation hardening and dislocation channelling leading to local plastic strain softening. Using a simple single-slip model, loops were shown to demonstrably elevate flow stress, observed to increase with increasing loop density in accord with experimental observations of irradiation hardening. Furthermore, the important role of the out-of-plane loop segments, captured by the restoring force obtained from the 3D analyses, was revealed. It is concluded that the 2.5D model introduced here, which will be described in greater detail in a forthcoming publication, captures many of the salient effects of dislocation-loop interactions, hence provides a basis for examining these effects in detail in larger, more realistic boundary value problems relevant to irradiation damage in nuclear power applications.

CRediT authorship contribution statement

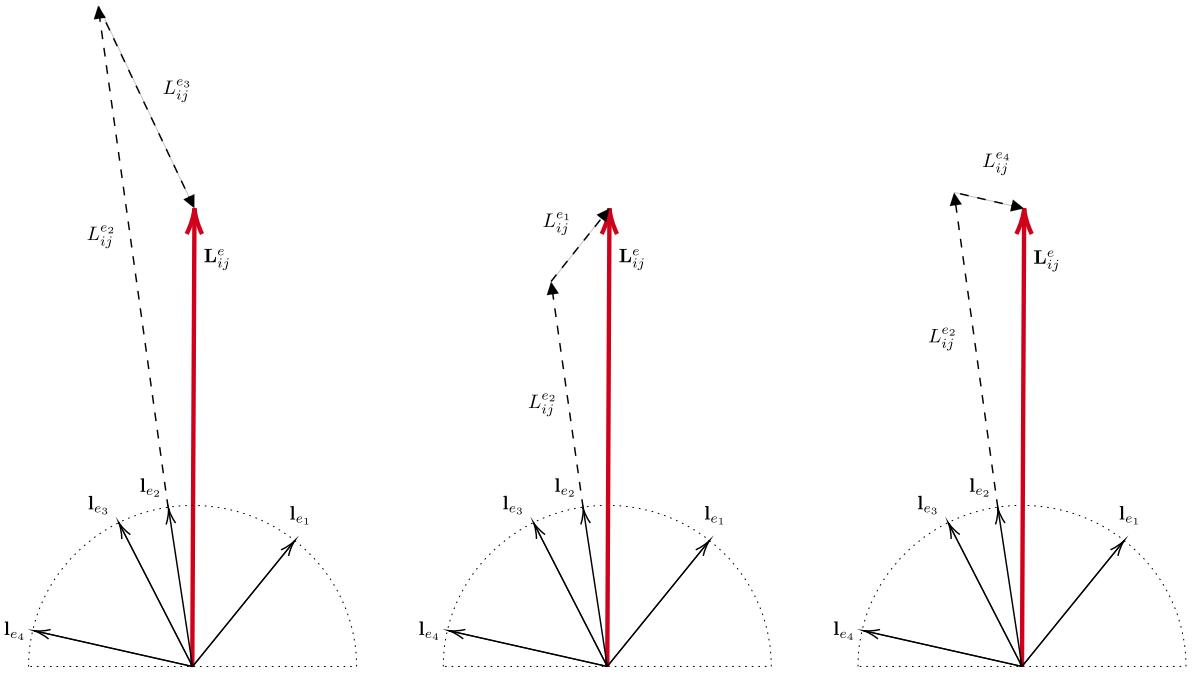
Daniel Hortelano-Roig: Conceptualization, Methodology, Software, Validation, Formal analysis, Investigation, Data curation, Writing – original draft, Writing – review & editing, Visualization. **Rakesh Kumar:** Conceptualization, Methodology, Software, Validation, Formal analysis, Investigation, Writing – original draft, Writing – review & editing, Visualization. **Daniel S. Balint:** Conceptualization, Methodology, Resources, Writing – review & editing, Supervision, Project administration, Funding acquisition. **Edmund Tarleton:** Conceptualization, Resources, Writing – review & editing, Supervision, Project administration.

Declaration of competing interest

The authors declare that they have no known conflicts of interest.

Data availability

Data will be made available on request.



(a) Decomposition outcome of simple projection-based minimisation algorithm. See Appendix A.2.

(b) Decomposition outcome of perimeter minimisation algorithm (which is functionally equivalent to the L^1 norm minimisation algorithm). See Appendix A.4.

(c) Decomposition outcome of altered simple projection-based minimisation algorithm. See Appendix A.3.

Fig. A.13. Optimal edge vector decompositions given a set of basis line vectors according to different algorithms. Basis line vectors can be depicted without loss of generality to be emanating from a single source and lying at the edges of a half unit circle.

Acknowledgements

We would like to acknowledge the insightful discussions with Dr. Melyvn Larranaga regarding dislocation slip in HCP materials and Mr. William van Noordt regarding vector decomposition algorithms. Funding was provided through the EPSRC MIDAS grant EP/S01702X/1 and ET acknowledges financial support through a UKAEA/Royal Academy of Engineering Senior Research Fellowship.

Appendix A. Length vector decomposition

The general optimisation problem to solve is

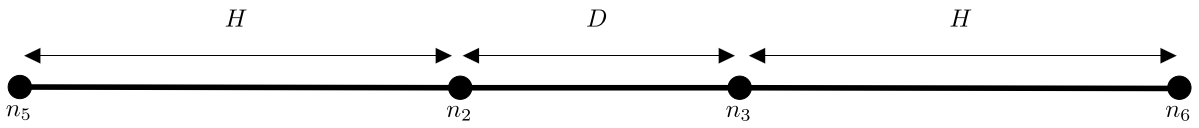
$$\underset{\{L_{ij}^{e_q}\}}{\arg\min}\, \mathcal{F}(\{L_{ij}^{e_q}\}) \quad \text{such that} \quad \boldsymbol{L}_{ij}^{e} = L_{ij}^{e_1}\boldsymbol{l}_{ij}^{e_1} + \cdots + L_{ij}^{e_N}\boldsymbol{l}_{ij}^{e_N} \quad \text{and} \quad \bigcup_{q=1}^{N}\{\boldsymbol{l}_{ij}^{e_q}\} \subseteq \mathbb{R}^2 \tag{A.1}$$

where the N unit vectors contained in the set $\bigcup_q\{\boldsymbol{l}^{e_q}\}$ are in general linearly dependent and lie on the same two-dimensional plane with normal vector $\boldsymbol{b}_{ij}$. There are several potential candidates for an algorithm which finds an optimal decomposition for the edge component $\boldsymbol{L}_{ij}^{e}$. These algorithms are formally distinguished by the choice of the objective function $\mathcal{F}$. For the following sections, let $\boldsymbol{L} = (L_{ij}^{e_1}, \dots, L_{ij}^{e_N})^{\intercal} \in \mathbb{R}^N$ and $\mathcal{L} = (\boldsymbol{l}^{e_1}, \dots, \boldsymbol{l}^{e_N}) \in \mathbb{R}^{3\times N}$ such that $\boldsymbol{L}_{ij}^{e} = \mathcal{L}\boldsymbol{L}$.

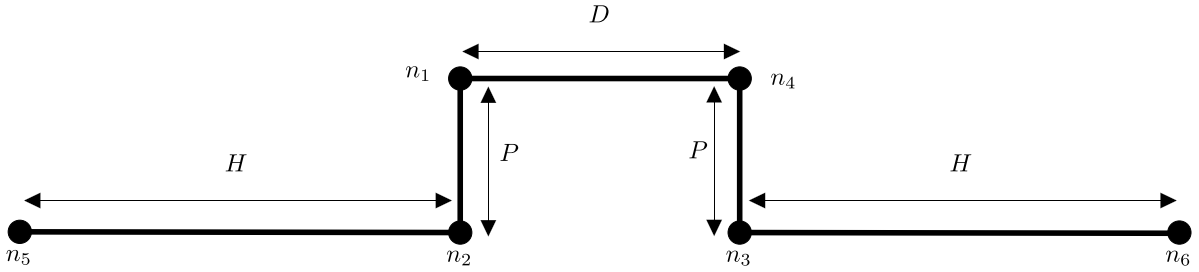
A.1. Norm minimisation

Problem (A.1) may be solved using the L^p norm objective functions $\mathcal{F}(\{L_{ij}^{e_q}\}) = (\sum_k^N |L_{ij}^{e_k}|^p)^{1/p}$. The HCP mobility law developed by Aubry et al. (2016) uses the L^1 norm objective function. It can be shown that the standard L^1 norm minimisation problem may be cast into a linear programming format given by

$$\underset{\boldsymbol{L},\boldsymbol{H}}{\arg\min}\begin{bmatrix}\mathbf{0} & \mathbf{1}\end{bmatrix}\begin{bmatrix}\boldsymbol{L}\\ \boldsymbol{H}\end{bmatrix} \quad \text{such that} \quad \begin{bmatrix}I_N & -I_N\\ -I_N & -I_N\end{bmatrix}\begin{bmatrix}\boldsymbol{L}\\ \boldsymbol{H}\end{bmatrix} \le \begin{bmatrix}\mathbf{0}\\ \mathbf{0}\end{bmatrix},\ \begin{bmatrix}\mathcal{L} & \mathbf{0}\end{bmatrix}\begin{bmatrix}\boldsymbol{L}\\ \boldsymbol{H}\end{bmatrix} = \boldsymbol{L}_{ij}^{e},\ \begin{bmatrix}\boldsymbol{L}\\ \boldsymbol{H}\end{bmatrix} \ge \begin{bmatrix}-\infty\\ \mathbf{0}\end{bmatrix} \tag{A.2}$$



(a) Edge dislocation.



(b) Edge dislocation with an acquired double super-jog. Only the $P = D$ case is considered in this paper.

Fig. B.14. Diagrams of an edge dislocation before and after a collision with a prismatic loop has occurred.

where $\mathbf{0} = (0, \dots, 0)^\intercal$, $\mathbf{1} = (1, \dots, 1)^\intercal$, $\boldsymbol{\infty} = (\infty, \dots, \infty)^\intercal$, the entries of $\boldsymbol{H} \in \mathbb{R}^N$ and $\boldsymbol{L}$ are related via $H_i = |L_i|$, and I_N denotes the $N \times N$ identity matrix. This linear program may then be solved by applying standard optimisation techniques or software packages such as the MATLAB function `linprog`.

A.2. Simple projection-based optimisation

A simple alternative to the L^1 norm minimisation algorithm proceeds as follows. First, the set consisting of the projections $\bigcup_{q=1}^{N} \{\beta_q = |\boldsymbol{L}_{ij}^e \cdot \boldsymbol{l}^{e_q}|\}$ is generated. $\boldsymbol{L}_{ij}^e$ is then decomposed with respect to the basis $\{\boldsymbol{l}^{e_a}, \boldsymbol{l}^{e_b}\}$ consisting of two basis vectors which correspond to the two greatest projection magnitudes β_a and β_b.

See Fig. A.13(a) for a depiction of a decomposition outcome of this algorithm. The corresponding decomposition outcome does not necessarily favour the minimisation of the effective length of the segment components which contribute to the segment drag, and can thus lead to artefacts. It can be shown that this simple optimisation algorithm in general yields a different decomposition compared to the L^1 norm algorithm (see Fig. A.13(b) for a counter-example).

A.3. Altered simple projection-based optimisation

A minor amendment to the simple projection-based algorithm described above can yield a significant improvement with regards to minimising mobility-related artefacts. The procedure is as follows. First, as in the original algorithm, compute the set of projections $\bigcup_{q=1}^{N} \{\beta_q = |\boldsymbol{L}_{ij}^e \cdot \boldsymbol{l}^{e_q}|\}$. Next, decompose $\boldsymbol{L}_{ij}^e$ with respect to the basis $\{\boldsymbol{l}^{e_a}, \boldsymbol{l}^{e_b}\}$ consisting of two basis vectors: one corresponding to the greatest projection magnitude β_a, and the other corresponding to the smallest projection magnitude β_b. See Fig. A.13(c) for a depiction of a decomposition outcome of this algorithm.

A.4. Perimeter minimisation

In order to reduce mobility-related artefacts, it may be favourable to select an algorithm which instead minimises the perimeter of triangles generated by $\boldsymbol{L}_{ij}^e$ and its two decomposed components. This is precisely what the L^1 norm minimisation algorithm achieves, but an equivalent deterministic algorithm is presented in the following. First, the set consisting of the projections $\bigcup_{q=1}^{N} \{\beta_q = |\boldsymbol{L}_{ij}^e \cdot \boldsymbol{l}^{e_q}|\}$ is generated. The greatest projection magnitude β_a is then selected and stored. Next, a copy of the edge vector, $\boldsymbol{P}$, is rotated by 90 degrees anti-clockwise with respect to the Burgers vector, and the sign value $s_a = \text{sign}(\boldsymbol{P} \cdot \boldsymbol{l}^{e_a})$ is calculated and stored. The set consisting of the projections $\bigcup_{q=1, q\neq a}^{N} \{\eta_q = s_a \boldsymbol{P} \cdot \boldsymbol{l}^{e_q}\}$ is generated. The line vector $\boldsymbol{l}^{e_b}$ corresponding to the greatest projection which is less than zero, η_b, is then selected. $\boldsymbol{L}_{ij}^e$ is then decomposed with respect to the basis $\{\boldsymbol{l}^{e_a}, \boldsymbol{l}^{e_b}\}$.

The above algorithm will result in a decomposition outcome which selects the basis line vectors with the two greatest projection magnitudes which are on opposite sides of $\boldsymbol{L}_{ij}^e$ as seen in Fig. A.13(b).

Appendix B. Double super-jog dragging effect

Consider the two following cases: (1) a straight edge dislocation with a nodal arrangement as shown in Fig. B.14(a), and (2) an edge dislocation which has acquired a double super-jog as in Fig. B.14(b). Suppose that in both cases a uniform external resolved shear stress τ is applied, and that each structure has a Burgers vector magnitude b. In case (1), the forces inducing motion in the

network will be entirely due to the external stress. For the moment, ignore nodal dynamics acting in the climb and line directions, and thus assume that all nodal forces and velocities act along glide directions. The force acting on node n_2 is given by

$$f_2^{\text{edge}} = \frac{\tau b}{2}(H + D) \tag{B.1}$$

This will be balanced by Eq. (16), which can be expanded to obtain

$$f_2^{\text{edge}} = \frac{1}{2}\left(H B_{25} + D B_{32}\right) v_2^{\text{edge}} \tag{B.2}$$

where B_{25} and B_{32} are the glide drag coefficients of segments Γ_{25} and Γ_{32}, respectively. Assuming that $B_{25} = B_{32}$, and after balancing Eqs. (B.1) and (B.2), one obtains

$$v_2^{\text{edge}} = \frac{\tau b}{B_{32}} \tag{B.3}$$

In case (2), the elastic fields generated by the structure do not induce motion at this tilt angle (i.e. zero) as shown by Fig. 6. Therefore, the forces inducing motion will be entirely due to the external stress, as in case (1). Performing once again a balance of forces, and assuming that $H \to \infty$ and $D = P$, one obtains an expression for the velocities of node n_1 and n_2 given respectively by

$$v_1^{\text{dsg}} = \frac{\tau b}{\left(B_{41} + B_{12}\right)} \tag{B.4}$$

and

$$v_2^{\text{dsg}} = \frac{\tau b}{\left(B_{41}\right)} \tag{B.5}$$

Assuming that $B_{41} = B_{32}$, it is evident that $v_1^{\text{dsg}} < v_2^{\text{dsg}} = v_2^{\text{edge}}$. This will result in segments Γ_{25} and, via symmetry, Γ_{63}, to experience a greater mobility than segment Γ_{41}. As segment Γ_{41} is dragged behind and induces a non-zero tilt angle in the structure, the elastic fields generated will act to induce stability such that segments Γ_{25} and Γ_{63} experience a restorative force opposing their direction of motion. This effect will persist until a tilt angle of zero is achieved, after which this process will occur once again. The net effect is a reduction in the mobility of the entire structure.

References

Adamson, R., 2000. Effects of neutron irradiation on microstructure and properties of zircaloy. In: Moan, G. (Ed.), Zirconium in the Nuclear Industry: Twelfth International Symposium. ASTM International, West Conshohocken, PA, pp. 15–31.

Arsenlis, A., Cai, W., Tang, M., Rhee, M., Oppelstrup, T., Hommes, G., Pierce, T.G., Bulatov, V.V., 2007. Enabling strain hardening simulations with dislocation dynamics. Modelling Simul. Mater. Sci. Eng. 15 (6), 553–595.

Aubry, S., Rhee, M., Hommes, G., Bulatov, V.V., Arsenlis, A., 2016. Dislocation dynamics in hexagonal close-packed crystals. J. Mech. Phys. Solids 94, 105–126.

Bacon, D.J., 1966. The elastic energies of elliptical dislocation loops. Philos. Mag.: J. Theor. Exp. Appl. Phys. 14 (130), 715–729.

Bacon, D., Osetsky, Y., 2005. Modelling dislocation–obstacle interactions in metals exposed to an irradiation environment. Mater. Sci. Eng. A 400–401, 353–361, Dislocations 2004.

Bacon, D., Osetsky, Y., Rodney, D., 2009. In: Hirth, J., Kubin, L. (Eds.), Chapter 88 Dislocation–Obstacle Interactions at the Atomic Level. In: Dislocations in Solids, vol. 15, Elsevier, pp. 1–90.

Bacon, D.J., Osetsky, Y.N., Rong, Z., 2006. Computer simulation of reactions between an edge dislocation and glissile self-interstitial clusters in iron. Phil. Mag. 86 (25–26), 3921–3936.

Balint, D.S., Deshpande, V.S., Needleman, A., der Giessen, E.V., 2005. Discrete dislocation plasticity analysis of crack-tip fields in polycrystalline materials. Phil. Mag. 85 (26–27), 3047–3071.

Borde, M., Dupuy, L., Pivano, A., Michel, B., Rodney, D., Amodeo, J., 2023. Interaction between 1/2⟨110⟩{001} dislocations and {110} prismatic loops in uranium dioxide: Implications for strain-hardening under irradiation. Int. J. Plast. 168, 103702.

Bulatov, V., Cai, W., 2006. Computer Simulations of Dislocations. In: Osmm Series, OUP Oxford.

Cai, W., Arsenlis, A., Weinberger, C.R., Bulatov, V.V., 2006. A non-singular continuum theory of dislocations. J. Mech. Phys. Solids 54 (3), 561–587.

Cai, W., Bulatov, V.V., 2004. Mobility laws in dislocation dynamics simulations. Mater. Sci. Eng. A 387–389, 277–281, 13th International Conference on the Strength of Materials.

Cline, A.K., Moler, C.B., Stewart, G.W., Wilkinson, J.H., 1979. An estimate for the condition number of a matrix. SIAM J. Numer. Anal. 16 (2), 368–375.

Clouet, E., 2012. Screw dislocation in zirconium: An *ab initio* study. Phys. Rev. B 86 (14), 144104.

Dai, C., Balogh, L., Yao, Z., Daymond, M.R., 2017. The habit plane of ⟨a⟩-type dislocation loops in α-zirconium: an atomistic study. Phil. Mag. 97 (12), 944–956.

Deshpande, V.S., Balint, D.S., Needleman, A., der Giessen, E.V., 2006. Size effects in single asperity frictional contacts. Modelling Simul. Mater. Sci. Eng. 15 (1), S97.

Drouet, J., Dupuy, L., Onimus, F., Mompiou, F., Perusin, S., Ambard, A., 2014. Dislocation dynamics simulations of interactions between gliding dislocations and radiation induced prismatic loops in zirconium. J. Nucl. Mater. 449 (1), 252–262.

Duan, Z., Yang, H., Satoh, Y., Murakami, K., Kano, S., Zhao, Z., Shen, J., Abe, H., 2017. Current status of materials development of nuclear fuel cladding tubes for light water reactors. Nucl. Eng. Des. 316, 131–150.

Erel, C., Po, G., Crosby, T., Ghoniem, N., 2017. Generation and interaction mechanisms of prismatic dislocation loops in FCC metals. Comput. Mater. Sci. 140, 32–46.

Giessen, E.V.d., Needleman, A., 1995. Discrete dislocation plasticity: a simple planar model. Modelling Simul. Mater. Sci. Eng. 3 (5), 689–735, Publisher: IOP Publishing.

Groh, S., Zbib, H.M., 2009. Advances in Discrete Dislocations Dynamics and Multiscale Modeling. J. Eng. Mater. Technol. 131 (4), 041209.

Higgy, H., Hammad, F., 1972. Effect of neutron irradiation on the tensile properties of zircaloy-2 and zircaloy-4. J. Nucl. Mater. 44 (2), 215–227.

Hirth, J., Lothe, J., 1982. Theory of Dislocations. In: A Wiley-Interscience publication, Wiley.

Hull, D., Bacon, D., 2011a. 6 - dislocations in other crystal structures. In: Hull, D., Bacon, D. (Eds.), Introduction To Dislocations (Fifth Edition), Fifth Butterworth-Heinemann, Oxford, pp. 109–136.

Hull, D., Bacon, D., 2011b. Introduction To Dislocations. In: Materials science and technology, Elsevier Science.
Jostsons, A., Kelly, P., Blake, R., 1977. The nature of dislocation loops in neutron irradiated zirconium. J. Nucl. Mater. 66 (3), 236–256.
Kelly, P.M., Blake, R.G., 1973. The characterization of dislocation loops in neutron irradiated zirconium. Philos. Mag.: J. Theor. Exp. Appl. Phys. 28 (2), 415–426.
Khater, H., Bacon, D., 2010. Dislocation core structure and dynamics in two atomic models of α-zirconium. Acta Mater. 58 (8), 2978–2987.
Kroupa, F., Hirsch, P.B., 1964. Elastic interaction between prismatic dislocation loops and straight dislocations. Discuss. Faraday Soc. 38, 49–55.
Kubin, L.P., Kratochvil, J., 2000. Elastic model for the sweeping of dipolar loops. Phil. Mag. A 80 (1), 201–218, Publisher: Taylor & Francis _eprint.
Li, M., Tian, X., Jiang, W., Wang, Q., Fan, H., 2023. Mechanism of strain hardening of magnesium single-crystals: Discrete dislocation dynamics simulations. J. Mech. Phys. Solids 173, 105238.
Liu, X.-Y., Biner, S., 2008. Molecular dynamics simulations of the interactions between screw dislocations and self-interstitial clusters in body-centered cubic fe. Scr. Mater. 59 (1), 51–54.
Lubarda, V.A., Blume, J.A., Needleman, A., 1993. An analysis of equilibrium dislocation distributions. Acta metall. mater. 41 (2), 625–642.
Luft, A., 1991. Microstructural processes of plastic instabilities in strengthened metals. Prog. Mater. Sci. 35 (2), 97–204.
Mussi, A., Addad, A., Onimus, F., 2021. Dislocation electron tomography: A technique to characterize the dislocation microstructure evolution in zirconium alloys under irradiation. Acta Mater. 213, 116964.
Nomoto, A., Soneda, N., Takahashi, A., Ishino, S., 2005. Interaction analysis between edge dislocation and self interstitial type dislocation loop in BCC iron using molecular dynamics. Mater. Trans. 46 (3), 463–468.
Northwood, D., Gilbert, R., Bahen, L., Kelly, P., Blake, R., Jostsons, A., Madden, P., Faulkner, D., Bell, W., Adamson, R., 1979. Characterization of neutron irradiation damage in zirconium alloys — an international "round-robin" experiment. J. Nucl. Mater. 79 (2), 379–394.
Onimus, F., Béchade, J., 2012. 4.01 - Radiation effects in zirconium alloys. In: Konings, R.J. (Ed.), Comprehensive Nuclear Materials. Elsevier, Oxford, pp. 1–31.
Onimus, F., Béchade, J.L., Gilbon, D., 2013. Experimental Analysis of Slip Systems Activation in Neutron-Irradiated Zirconium Alloys and Comparison with Polycrystalline Model Simulations. Metall. Mater. Trans. A 44 (1), 45–60.
Onimus, F., Monnet, I., Béchade, J.L., Prioul, C., Pilvin, P., 2004. A statistical TEM investigation of dislocation channeling mechanism in neutron irradiated zirconium alloys. J. Nucl. Mater. 328 (2), 165–179.
Po, G., Cui, Y., Rivera, D., Cereceda, D., Swinburne, T.D., Marian, J., Ghoniem, N., 2016. A phenomenological dislocation mobility law for bcc metals. Acta Mater. 119, 123–135.
Reali, L., Wenman, M.R., Sutton, A.P., Balint, D.S., 2021. Plasticity of zirconium hydrides: a coupled edge and screw discrete dislocation model. J. Mech. Phys. Solids 147, 104219.
Ribis, J., Onimus, F., Béchade, J.-L., Doriot, S., Cappelaere, C., Lemaignan, C., Barbu, A., Rabouille, O., Limback, M., Kammenzind, B., Dean, S., 2008. Experimental and modeling approach of irradiation defects recovery in zirconium alloys: Impact of an applied stress. J. Astm Int. 5.
Rodney, D., 2004. Molecular dynamics simulation of screw dislocations interacting with interstitial frank loops in a model FCC crystal. Acta Mater. 52 (3), 607–614.
Serra, A., Bacon, D.J., 2013. Atomic-level computer simulation of the interaction between dislocations and interstitial loops in α-zirconium. Modelling Simul. Mater. Sci. Eng. 21 (4), 045007.
Shi, X., Dupuy, L., Devincre, B., Terentyev, D., Vincent, L., 2015. Interaction of $\langle 100 \rangle$ dislocation loops with dislocations studied by dislocation dynamics in α-iron. J. Nucl. Mater. 460, 37–43.
Sills, R.B., Aubry, S., 2018. Line dislocation dynamics simulations with complex physics. In: Andreoni, W., Yip, S. (Eds.), Handbook of Materials Modeling : Methods: Theory and Modeling. Springer International Publishing, Cham, pp. 1–23.
Sills, R.B., Kuykendall, W.P., Aghaei, A., Cai, W., 2016. Fundamentals of dislocation dynamics simulations. In: Weinberger, C.R., Tucker, G.J. (Eds.), Multiscale Materials Modeling for Nanomechanics. In: Springer Series in Materials Science, Springer International Publishing, Cham, pp. 53–87.
Srivastava, K., El-Awady, J.A., 2017. Deformation of magnesium during c-axis compression at low temperatures. Acta Mater. 133, 282–292.
Starikov, S., Tseplyaev, V., 2020. Two-scale simulation of plasticity in molybdenum: Combination of atomistic simulation and dislocation dynamics with non-linear mobility function. Comput. Mater. Sci. 179, 109585.
Tarleton, E., Balint, D.S., Gong, J., Wilkinson, A.J., 2015. A discrete dislocation plasticity study of the micro-cantilever size effect. Acta Mater. 88, 271–282.
Tenckhoff, E., 1988. Deformation Mechanisms, Texture, and Anisotropy in Zirconium and Zircaloy.
Terentyev, D., Grammatikopoulos, P., Bacon, D., Osetsky, Y., Chaouadi, R., 2008. Simulation of the interaction between an edge dislocation and a $\langle 100 \rangle$ interstitial dislocation loop in α-iron. Acta Mater. 56 (18), 5034–5046.
University of Oxford Materials, 2021. EasyDD. https://github.com/TarletonGroup/EasyDD.
Voskoboynikov, R., Osetsky, Y., Bacon, D., 2005. Self-interstitial atom clusters as obstacles to glide of $1/3\langle 11\bar{2}0\rangle\{1\bar{1}00\}$ edge dislocations in α-zirconium. Mater. Sci. Eng. A 400–401, 54–58, Dislocations 2004.
Wickham, L.K., Schwarz, K.W., Stölken, J.S., 1999. Rules for Forest Interactions between Dislocations. Phys. Rev. Lett. 83 (22), 4574–4577, Publisher: American Physical Society.
Wolfer, W.G., Okita, T., Barnett, D.M., 2004. Motion and rotation of small glissile dislocation loops in stress fields. Phys. Rev. Lett. 92, 085507.
Xu, L., Xiao, Y., van Sandwijk, A., Xu, Q., Yang, Y., 2015. Production of nuclear grade zirconium: A review. J. Nucl. Mater. 466, 21–28.
Yagnik, S., Garde, A., 2019. Chapter 7 - zirconium alloys for LWR fuel cladding and core internals. In: Odette, G.R., Zinkle, S.J. (Eds.), Structural Alloys for Nuclear Energy Applications. Elsevier, Boston, pp. 247–291.
Zhuang, Z., Liu, Z., Cui, Y., 2019. Chapter 7 - discrete-continuous model of crystal plasticity at the submicron scale. In: Zhuang, Z., Liu, Z., Cui, Y. (Eds.), Dislocation Mechanism-Based Crystal Plasticity. Academic Press, pp. 177–217.